# Sensor-size-related attenuation correction of wall pressure spectra measurements

🆔 **Nan Hu** (胡楠)

View Online    Export Citation    CrossMark

**ARTICLES YOU MAY BE INTERESTED IN**

# Sensor-size-related attenuation correction of wall pressure spectra measurements

View Online    Export Citation    CrossMark

Nan Hu (胡楠)[a] iD

## AFFILIATIONS

Department of Technical Acoustics, German Aerospace Center (DLR), Lilienthalplatz 7, Brunswick 38108, Germany

[a]Author to whom correspondence should be addressed: nan.hu@dlr.de

## ABSTRACT

A correction model is presented for sensor-size-related high-frequency attenuation when measuring the wall pressure fluctuations beneath turbulent boundary layers. The model is developed based on the wall pressure spectra measured on a flat plate model using sensors of different sizes and types. The measurement covers the range of Reynolds numbers, $Re_\theta$, based on the momentum thickness between 1500 and 11 400, including flows with adverse and favorable pressure gradients, which were produced by a National Advisory Committee for Aeronautics (NACA) 0012 airfoil installed above the flat plate. The present model follows the principle of the Corcos correction and is expressed with a simple mathematical form. Major improvements compared with the Corcos correction are made with regard to determining the effective sensing area and the convection velocity for a specific sensor. With the help of convection velocity modeling, the present correction model can be applied to flows in pressure gradients with high accuracy. To assess the generality of the assumptions, the model is used to correct the wall pressure spectra measured at different test facilities with different sensor types, covering a large range of Reynolds numbers, $1.6 \times 10^3 < Re_\theta < 1.19 \times 10^5$.

## I. INTRODUCTION

A finite size of practical sensors limits the accurate measurement of wall pressure fluctuations at high frequencies. The problem arises from signal averaging over a sensor surface and has been reported in many research works.[1–6] Typically, one can choose a flush-mounted or a pinhole-mounted configuration.[7–11] With a pinhole-mounting, the spatial-averaging effect can be minimized due to a significantly reduced sensing area. However, in practice, such potential benefit of the pinhole configuration is most likely limited by the Helmholtz resonance. To increase the resonance frequency, a small sensor is often required which gives the reduced volume behind the pinhole. For a flush-mounted sensor, significant spectral attenuation will be measured at high frequencies because the sensor size is too large compared to the incident wavelength of the high-frequency pressure fluctuations.

This attenuation effect was systematically studied by Corcos,[1] who was the first to establish the relationship between the sensor size and the corresponding spectral attenuation from theory. The attenuation was calculated based on a semi-empirical model of the wall pressure coherence expressed as a function of $\omega r/U_c$, where $\omega$ is the angular frequency, $r$ and $U_c$ represent the sensor radius and the convection velocity of the pressure field, respectively. The obtained

attenuation spectrum was verified by Gilchrist and Strawderman,[12] White,[13] and Geib[14] in the frequency range of $\omega r/U_c < 3$ where the exponential growth of the attenuation is present. However, there has been a frequency shift of the attenuation spectra between different works, depending on the choice of $r$ and $U_c$.

In the study of Corcos,[1] a uniform spatial sensitivity over the sensor surface was assumed, which is not valid for actual sensors. Bruel and Rasmussen[15] measured the sensitivity distribution of a microphone membrane using a small electrostatic actuator and showed that the sensitivity is maximum near the center and approaches zero at the edge. Furthermore, Bruel and Rasmussen demonstrated that viscous damping is important for the microphone sensitivity at high frequencies and can significantly change the sensitivity distribution. Comparable results but without frequency characteristics were reported by Gilchrist and Strawderman[12] who measured the sensitivity distribution of two hydrophones by releasing pin loading from the piezoelectric transducer surface. It was suggested that a smaller area with constant sensitivity should be used as the "effective" sensing area that would have the same response level as the actual sensors. White[13] argued that for a better estimate of the effective sensing area, the wall pressure coherence has to be included in the calculation. The calculation results showed that the

attenuation is significantly reduced taking into account the non-uniform sensitivity, as a result of the reduced effective sensing area.

Furthermore, the determination of $U_c$ for different test conditions is important for applying the correction. However, this issue has rarely been discussed. Except for the frequency dependence, the magnitude of $U_c$ also depends on the convection distance,[7,8,16,17] indicating that the choice of $U_c$ may have to be sensor-size-dependent. Furthermore, pressure gradients can affect $U_c$. Especially, the adverse pressure gradient can significantly reduce the magnitude of $U_c$.[8,16,17] The reduced $U_c$ leads to a larger value of $\omega r/U_c$ that increases the attenuation level for a given frequency, especially at high frequencies.[18] However, there is a lack of knowledge on how to quantify the effects of convection distance and pressure gradients on $U_c$, making the correction difficult to apply in practice.

In the present work, the attenuation spectra are obtained for different sensor sizes and types, based on the wall pressure spectra measurements with flush- and pinhole-mounted sensors. The effect of non-uniform sensor sensitivity is theoretically discussed and the effective radius for different sensor types is suggested for practical applications. Furthermore, a convection velocity model is proposed, covering the effects of convection distance and pressure gradients. Finally, a correction model is proposed, which can be applied to flows with pressure gradients and commonly used sensor types. To assess the generality of the model, corrections are made for wall pressure spectra measured with four different sensor types from different test facilities.

## II. EXPERIMENTAL SETUP

The experiment was conducted in the Acoustic Wind Tunnel Braunschweig (AWB). The wind tunnel has a rectangular nozzle with a height of 1200 mm and a width of 800 mm, and can provide a maximum operating velocity of 65 m/s. A photograph of the experimental setup along with a side view sketch is shown in Fig. 1. A flat wooden plate, with a superelliptically shaped leading edge and a beveled trailing edge on its lower side, was placed 10 mm downstream of the nozzle exit at the nozzle mid-height position. The plate surface was aligned with the flow direction. The length and thickness of the plate are 1350 and 42 mm, respectively. The plate span is 1300 mm, which is 250 mm wider than the nozzle exit on each side. This prevents side-edge interaction with the open-jet shear layers. Both sides of the plate were tripped with 0.3-mm-thick zigzag trip strips 120 mm behind the leading edge. The trailing edge of the plate was extended by foam serrations to minimize vortex shedding and to reduce trailing edge noise.[19] Furthermore, from the previous test with the same setup,[8] contamination was measured at low frequencies of the wall pressure spectra which is assumed to be related to the open-jet shear layers. The nozzle exit was extended above the plate by using sidewalls to reduce the thickness of the open-jet shear layers in the measurement area, in an attempt to minimize the shear-layer impact. However, when compared to the previous results without the side walls,[8] no significant reduction of the contamination can be identified.

Pressure gradients were introduced in the boundary layers by placing a National Advisory Committee for Aeronautics (NACA) 0012 airfoil with 400 mm chord length and 1800 mm span width above the plate. The airfoil with its leading edge at $x = 760$ mm ($x = 0$ denotes the leading edge of the plate) was installed 120 mm above the plate relative to the wing's chord at the geometric angle of attack (AOA) of 0°. The rotation axis was at 41% of the chord length. The AOA of the airfoil was varied between $-14°$ and $14°$ to produce the desired flow conditions. Both sides of the airfoil were tripped at 20% chord length with 0.4-mm zigzag trip strips to avoid a possible laminar vortex shedding noise at the largest AOA. To reduce the trailing edge noise of the airfoil, the trailing edge was extended with a 50-mm-long brush.[20] Static pressure distributions on the pressure and suction sides of the airfoil were measured with 46 static pressure ports.

A 370-mm-long, 270-mm-wide, and 5-mm-thick aluminum panel was placed at mid-span in the streamwise location of 890 mm $\leq x \leq$ 1260 mm. The panel was equipped with 26 static pressure ports and different types of dynamic pressure sensors. The static pressure ports covered a range of 290 mm in the streamwise direction and 180 mm in the spanwise direction. To measure the wall pressure fluctuations, seven pinhole-mounted Kulite sensors, model LQ-062–5psi (absolute operational mode) without protection screens, with a pinhole diameter of 0.5 mm were applied in the range of 1105 mm
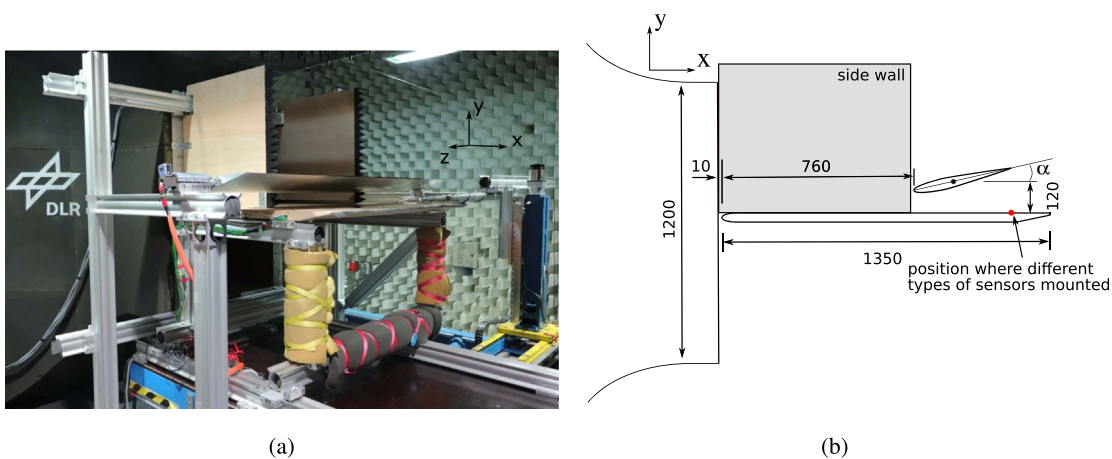


(a)  (b)

**FIG. 1.** Test setup of the wall pressure spectra measurement, (a) photograph of the flat plate model with a NACA 0012 airfoil and side walls installed in AWB. The x, y, and z axes represent the flow direction, wall-normal direction, and spanwise direction, respectively; (b) side view sketch.
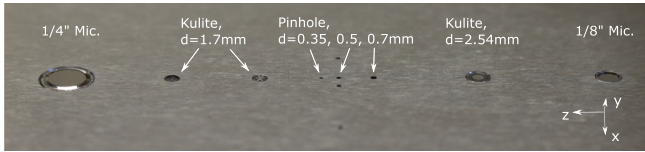
**FIG. 2.** Different types of sensors mounted at $x = 1170$ mm.

$\le x \le 1210$ mm at mid-span of the plate, that is, $z = 0$. In the spanwise direction at $x = 1170$ mm, two other pinholes with the same type of Kulites, but different diameters of 0.35 and 0.7 mm were applied, see Fig. 2. The depth of all pinholes was 0.4 mm. Furthermore, three Kulite sensors and two condenser microphones were flush mounted in a range of $|z| \le 31$ mm. The sensors from left to right shown in Fig. 2 are B&K 1/4-in. pressure microphone, model 4136 without protection screen; Kulite sensor with a diameter of $d = 1.7$ mm, model XCQ-062-5psi (differential operational mode) without protection screen; Kulite sensor with $d = 1.7$ mm, model XCS-062–5psi (absolute operational mode) with B-screen (minholes placed in a circle on the screen); pinhole with $d = 0.35$ mm; pinhole with $d = 0.5$ mm; pinhole with $d = 0.7$ mm; Kulite sensor with $d = 2.54$ mm, model XT-140M-5psi (differential operational mode) with B-screen; and GRAS 1/8-in. pressure microphone, model 40DP without protection screen. The fluctuating pressures were recorded for 30 s with a sampling rate of 100 kHz using a 16-bit GBM Viper data acquisition system. To improve the signal-to-noise ratio, an external preamplifier (gain factor of 250) with a first-order high-pass filter (cutoff frequency at 270 Hz) was applied to the Kulite sensors.

The mean flow velocities were measured using a Dantec single-wire hotwire probe, model 55P11. The hotwire data were recorded with 10.3 s for each measurement point. A sampling rate of 50 kHz and a low-pass filter with cutoff frequency of 20 kHz were applied.

## III. RESULTS

### A. Boundary layer parameters

Figure 3(a) shows the streamwise pressure coefficient ($C_p$) distribution for zero, adverse and favorable pressure gradients (ZPG, APG, and FPG) flows with $U_\infty = 30$ m/s ($U_\infty$ denotes the free-stream velocity at the nozzle exit). For the configuration without the NACA airfoil, a nearly ZPG turbulent boundary layer (TBL) flow with a slight APG for $x > 1100$ mm was present. An APG at the measurement position was produced with a positive airfoil AOA, as illustrated in Fig. 1. With a negative AOA, a FPG flow condition was produced. Based on the measured static pressure of the airfoil, flow separation on the suction side was identified for the FPG cases with AOAs of $-12°$ and $-14°$. Note, there was no flow separation for the FPG II case with AOA = $-12°$, see Table I, which was achieved by tests starting with $U_\infty = 60$ m/s. Interestingly, the flow separation on the airfoil also affected the flow development on the flat plate, indicated by the different $C_p$ values between the FPG-12° and FPG II-12° cases.

The mean flow velocity was measured at the mid-span of the plate and at the streamwise position of $x = 1170$ mm, where the different types of sensors were mounted, see Fig. 2. Figure 3(b) shows the boundary layer profiles in wall units for ZPG flows with different velocities and APG and FPG flows with $U_\infty = 30$ m/s. The measured profiles collapse into the log law with $\kappa = 0.384$ and $C^+ = 4.17$ as suggested by Nagib et al.[21] A two-dimensional flow condition within the measurement area for ZPG, APG, and FPG cases was verified by a sufficiently weak spanwise variation of the TBL profile measured at $|z| \le 80$ mm.[22]

The relevant boundary layer parameters are summarized in Table I. To determine the boundary layer displacement thickness $\delta^*$ and momentum thickness $\theta$, the mean velocities for locations $y < 1$ mm are estimated using Spalding's wall law.[23] The values of the shape factor $H$ for the ZPG flows turn out to be slightly larger than the values collected in Ref. 21, probably due to the slight APG present in the measurement area, which also results in small positive values of
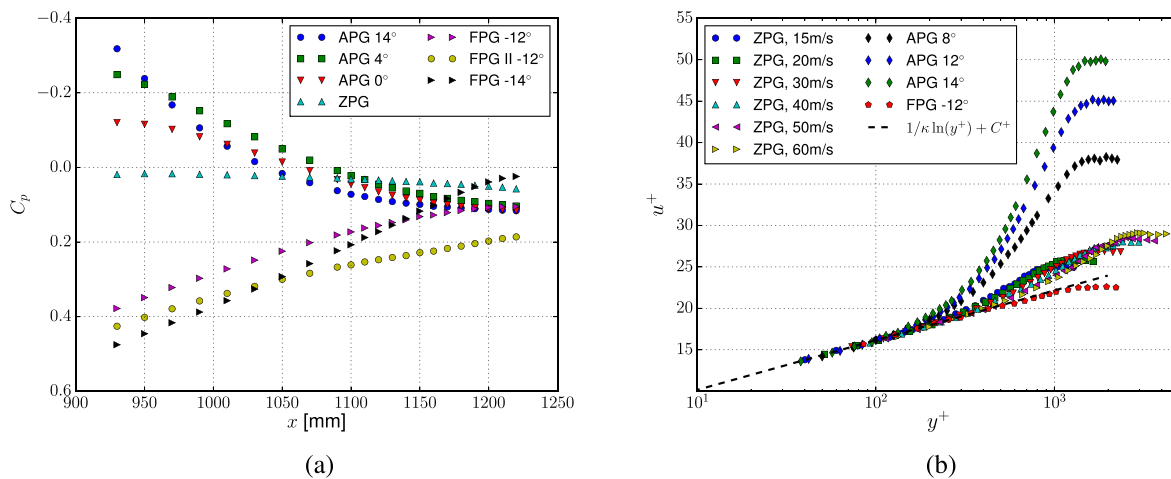


(a)



(b)

**FIG. 3.** (a) Cp distribution of selected flow conditions with $U_\infty = 30$ m/s; (b) mean velocity profiles in wall units for ZPG with different velocities and APG & FPG with $U_\infty = 30$ m/s.

**TABLE I.** Boundary layer parameters at $x = 1170$ mm.

| | $U_\infty$ (m/s) | $U_e$ (m/s) | $\delta$ (mm) | $\delta^*$ (mm) | $\theta$ (mm) | $H = \delta^*/\theta$ | $u_\tau$ (m/s) | $Re_\tau = u_\tau\delta/\nu$ | $Re_\theta = U_e\theta/\nu$ | $\beta_{\delta^*} = \frac{\delta^*}{\tau_w}\frac{dp}{dx}$ | $d^+ = u_\tau d/\nu$ |
|---|---|---|---|---|---|---|---|---|---|---|---|
| ZPG | 15 | 15.1 | 21.2 | 3.89 | 2.7 | 1.44 | 0.6 | 848 | 2700 | 0.23 | 14.0 |
| ZPG | 20 | 20.0 | 19.8 | 3.64 | 2.54 | 1.43 | 0.78 | 1020 | 3364 | 0.24 | 18.0 |
| ZPG | 30 | 29.7 | 19.3 | 3.45 | 2.44 | 1.41 | 1.11 | 1416 | 4799 | 0.26 | 25.7 |
| ZPG | 40 | 39.2 | 19.2 | 3.53 | 2.53 | 1.4 | 1.4 | 1781 | 6568 | 0.28 | 32.5 |
| ZPG | 50 | 48.5 | 18.2 | 3.23 | 2.3 | 1.41 | 1.71 | 2065 | 7387 | 0.26 | 39.7 |
| ZPG | 60 | 58.1 | 18.5 | 3.31 | 2.37 | 1.4 | 2.01 | 2458 | 9119 | 0.29 | 46.5 |
| FPG-10° | 20 | 17.6 | 17.5 | 2.57 | 1.87 | 1.37 | 0.76 | 887 | 2180 | −0.64 | 17.7 |
| FPG-12° | 20 | 18.6 | 14.4 | 1.84 | 1.37 | 1.34 | 0.87 | 826 | 1688 | −0.52 | 20.1 |
| FPG-12° | 30 | 29.0 | 14.3 | 1.71 | 1.3 | 1.31 | 1.29 | 1218 | 2497 | −0.26 | 29.8 |
| FPG-12° | 40 | 38.1 | 12.4 | 1.45 | 1.1 | 1.32 | 1.65 | 1358 | 2775 | −0.08 | 38.3 |
| FPG II-12° | 20 | 18.1 | 16.5 | 2.2 | 1.65 | 1.34 | 0.82 | 900 | 1978 | −0.54 | 19.1 |
| FPG-14° | 20 | 19.5 | 14.3 | 1.55 | 1.18 | 1.31 | 0.94 | 894 | 1524 | −0.86 | 21.9 |
| APG 0° | 20 | 18.8 | 21.9 | 4.42 | 2.9 | 1.52 | 0.66 | 957 | 3611 | 0.78 | 15.3 |
| APG 4° | 20 | 19.0 | 25.2 | 5.87 | 3.64 | 1.61 | 0.59 | 988 | 4580 | 1.56 | 13.7 |
| APG 6° | 20 | 18.9 | 27.5 | 6.73 | 4.06 | 1.66 | 0.56 | 1011 | 5082 | 1.91 | 12.9 |
| APG 8° | 15 | 14.2 | 31.2 | 8.19 | 4.73 | 1.73 | 0.4 | 820 | 4448 | 1.96 | 9.2 |
| APG 8° | 20 | 19.0 | 30.3 | 7.91 | 4.6 | 1.72 | 0.52 | 1039 | 5788 | 2.26 | 12.0 |
| APG 8° | 30 | 28.7 | 28.7 | 7.41 | 4.35 | 1.7 | 0.76 | 1435 | 8268 | 2.5 | 17.5 |
| APG 8° | 40 | 38.3 | 29.6 | 7.32 | 4.35 | 1.68 | 0.98 | 1919 | 11 033 | 2.77 | 22.7 |
| APG 10° | 20 | 19.0 | 33.3 | 9.3 | 5.15 | 1.8 | 0.47 | 1041 | 6480 | 2.73 | 10.9 |
| APG 12° | 15 | 14.2 | 36.9 | 11.0 | 5.84 | 1.88 | 0.34 | 833 | 5492 | 2.23 | 7.9 |
| APG 12° | 20 | 19.0 | 35.8 | 10.75 | 5.72 | 1.88 | 0.44 | 1036 | 7197 | 2.91 | 10.1 |
| APG 12° | 30 | 28.6 | 34.4 | 10.21 | 5.48 | 1.86 | 0.63 | 1444 | 10 379 | 3.34 | 14.7 |
| APG 12° | 40 | 37.6 | 31.6 | 9.8 | 5.24 | 1.87 | 0.82 | 1708 | 13 048 | 3.59 | 18.9 |
| APG 14° | 20 | 19.2 | 38.3 | 12.19 | 6.19 | 1.97 | 0.4 | 1022 | 7871 | 3.24 | 9.3 |
| APG 14° | 30 | 28.6 | 36.7 | 11.78 | 5.98 | 1.97 | 0.57 | 1393 | 11 326 | 3.85 | 13.3 |

the Clauser parameter $\beta_{\delta^*}$. The friction velocity $u_\tau$ is estimated according to the log-law fitting. The parameter $d^+$ is the normalized diameter calculated based on the pinhole diameter of $d = 0.35$ mm.

## B. Wall pressure one-point spectra

Figure 4(a) shows the measured wall pressure one-point spectra with all sensor types for ZPG at $U_\infty = 30$ m/s. Here, the one-point spectra denote the power spectral density (PSD). The spectra were calculated using a Hanning window with 8192 samples per window and 50% overlap, resulting in a frequency resolution of 12.2 Hz.

The result shows that the spectra were contaminated by different types of disturbances. For example, the Kulite sensors have a high level of electric noise between 45 and 50 dB. The high-frequency wall pressure spectra that fall below this level are covered by the electric noise. Furthermore, Helmholtz resonance was excited for the Kulite sensors with a pinhole construction or a B-screen. Note, in Fig. 4(a), the resonance can only be clearly identified for the pinhole-mounted Kulite sensors with $d = 0.35$ and 0.5 mm. For the other cases, the resonance is covered by the electric noise, which can be observed after subtraction of the noise [see Fig. 4(b)]. It is somewhat surprising that a strong disturbance occurs at low frequencies for the pinhole construction with $d = 0.7$ mm compared to the pinholes with $d \leq 0.5$ mm. It is

assumed that hydrodynamic disturbance was induced due to the "large" pinhole size. Furthermore, the disturbance could be measured because of the small pinhole depth and the close distance between the sensor chip and the pinhole.

Figure 5 illustrates problems related to the flush-mounting installation in the present test of three types. The left sketch shows a cavity problem for the 1/8-in. microphone and the Kulite sensor without screens, which occurred because the sensor rim is higher than the sensing area. The backward-facing step can cause a flow separation that will produce a strong low-frequency disturbance.[24] A stagnation point of the separation may be expected at around eight times the step height ($h$),[24,25] which indicates that the entire area of the Kulite sensor ($d = 1.7$ mm) would probably be affected by the separation. This may explain a more intense low-frequency disturbance measured by the Kulite sensor than the 1/8-in. microphone.

Furthermore, large chamfers were produced by manufacturing the holes for the Kulite sensor with $d = 2.54$ mm and for the 1/4-in. microphone, see the middle and right sketches in Fig. 5. The chamfer-induced disturbances at low and high frequencies measured by the Kulite sensor can be identified by compared to the spectra measured with the pinhole-mounted ($d = 0.35$ mm) Kulite sensor and the 1/8-in. microphone. Note, that a similar high-frequency disturbance but with
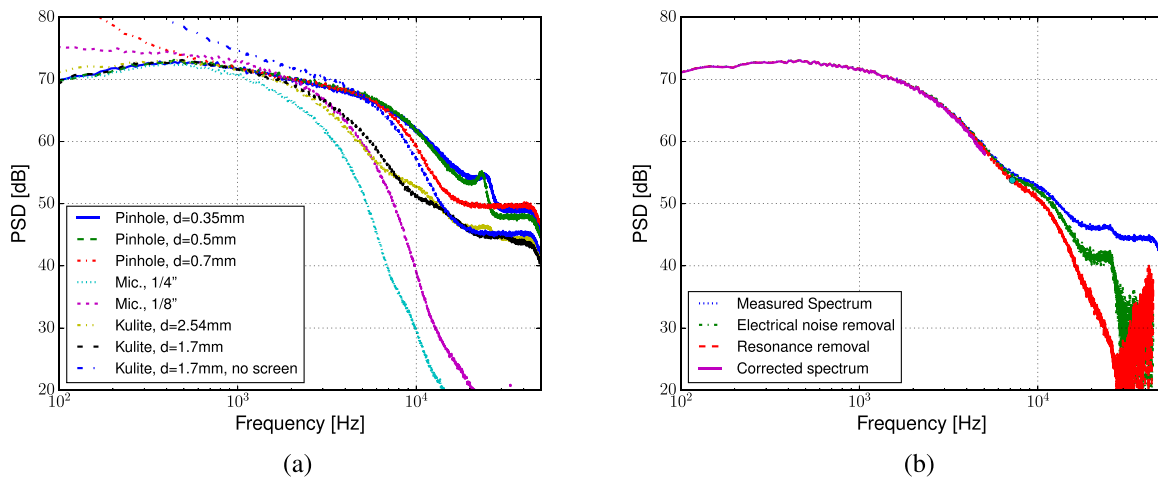
**FIG. 4.** (a) Measured wall pressure one-point spectra with all sensor types for ZPG with $U_\infty = 30$ m/s; (b) correction of high-frequency disturbances for the flush-mounted Kulite sensor with $d = 2.54$ mm.

a smaller magnitude was measured by the flush-mounted Kulite sensor with $d = 1.7$ mm, which has no noticeable chamfers (see Fig. 2). This indicates that even a very small surface discontinuity found directly in front of the sensor may cause a measurable high-frequency disturbance. There might be mid-frequency disturbance, which could be picked up by flush-mounted sensors with a larger chamfer.[18] However, such disturbance cannot be identified in the attenuated spectra due to its small level. There was no noticeable disturbance measured with the 1/4-in. microphone, which had the sloped protruding membrane. Golubev and Kuznetsov[26] measured the wall pressure spectra on sloped forward-facing steps with different slope angles and showed that a smaller angle could significantly reduce the disturbance magnitude. The disturbance could not be measured at 2.6 h behind the step with a step angle of 30° (similar to the 1/4-in. microphone case) and $\delta/h = 7$. For the present case ($\delta/h \simeq 100$), the disturbance would be smaller than that measured by Golubev and Kuznetsov, because a larger $\delta/h$ can significantly reduce the disturbance.[26] Thus, it is assumed that the step-induced disturbance would only affect the membrane border area and not disturb the measured spectra because of the very low sensitivity at the border area.

To extend the usable frequency range for the study of the sensor-size-related spectral attenuation, the high-frequency disturbances need to be eliminated. There are three types of disturbances: the electric noise, Helmholtz resonance, and flush-mounting-related noise. An example of such a correction for a flush-mounted Kulite sensor is given in Fig. 4(b). Note that the decibel subtraction should follow the time

sequence of the disturbance occurrence. First, the electrical noise is subtracted from the measured spectrum with the following expression:

$$L = 10 \log \left(10^{L_m/10} - 10^{L_{noise}/10}\right), \qquad (1)$$

where $L_m$ denotes the measured spectrum level. After subtracting the electric noise from the overall spectrum, the Helmholtz resonance can be identified. The subtracted spectrum becomes noisy at frequencies larger than 20 kHz due to a poor signal-to-noise ratio. Thus, frequencies are not considered for the correction at which the spectral level is less than 2 dB larger than the electric noise. This introduces a cutoff frequency for cases where the electrical noise restricts the frequency range, for example, the pinhole with $d = 0.7$ mm [see Fig. 4(a)]. Second, the Helmholtz resonance is corrected with the corresponding transfer function, which was previously determined with the help of a laser-generated point source (see Appendix A). Finally, one has to deal with the flush-mounting-related noise, which can be identified by inspecting sudden changes in the spectral shape marked in Fig. 4(b). From the marked frequency onward, it is assumed that the disturbance dominates the spectrum. It is most likely that this disturbance also affects the spectrum below this frequency. It can be assumed that the disturbance and the wall pressure have the same level at the marked frequency, that is, 3 dB smaller than the measured magnitude. This value is used in Eq. (1) to correct the spectrum below the marked frequency. Due to the high uncertainty of the assumed disturbance level, a cutoff frequency is defined with a threshold magnitude of 5 dB larger
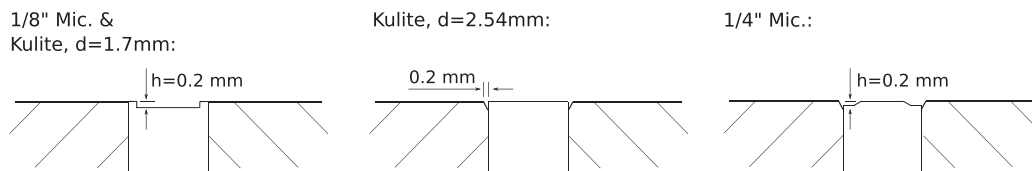


**FIG. 5.** Sketch of the flush-mounting-related problems.

than at the marked point. Frequencies larger than the cutoff frequency are not considered for the corrected spectrum.

Figure 6 shows the corrected spectra for ZPG with $U_\infty = 30, 60$ m/s and APG 12° and FPG-12° with $U_\infty = 30$ m/s that are obtained using the above procedure. The results show that a larger velocity increases the flush-mounting induced low-frequency disturbance, whereas for the APG flow condition the disturbance is significantly reduced except for the Kulite sensor without screen. This effect was also observed by Hu and Erbig,[18] where the flush-mounting-related disturbance was studied in more detail. Furthermore, additional contamination below 200 Hz can be observed (for the ZPG case with $U_\infty = 30$ m/s below 100 Hz). Note that the noise level is significantly increased by installing the NACA airfoil, which affects the development of the open-jet shear layer between the airfoil and the plate.[18] It indicates that this low-frequency noise is related to the open-jet shear layers.

Regarding the Helmholtz resonance correction, the corrected spectra shown in Fig. 6 illustrate that the resonance cannot be completely removed using the transfer function determined by the acoustic excitation (see Appendix A). Small peaks are still visible in the corrected spectra, and the correction accuracy depends on the pinhole size. Furthermore, the resonance is also flow-velocity dependent, as reported in Refs. 27–29. According to the limited success of the resonance correction, an additional cutoff frequency is applied to the pinhole-mounted sensors. More precisely, it is 20 kHz for the pinhole with $d = 0.35$ mm and 18 kHz for $d = 0.5$ mm, as illustrated in Fig. 6(a).

For the calculation of the sensor-size-related spectral attenuation, the corrected spectrum measured with the pinhole of $d = 0.35$ mm is chosen as the reference spectrum assumed to have no attenuation. However, even with such small pinhole size, attenuation of measured spectra could occur. Gravante et al.[6] showed that wall pressure spectral attenuation was measured at high frequencies in the $\omega^{-5}$ region[30] with a pinhole diameter $d^+ = u_\tau d/\nu > 18$. According to Table I, this threshold value is exceeded by many present test cases, for example, the ZPG cases with $U_\infty \geq 30$ m/s and most of the FPG cases. For high velocities ($U_\infty \geq 40$ m/s), the $\omega^{-5}$ region is removed from the corrected spectrum due to the cutoff frequency [see Fig. 6(b)]. For the
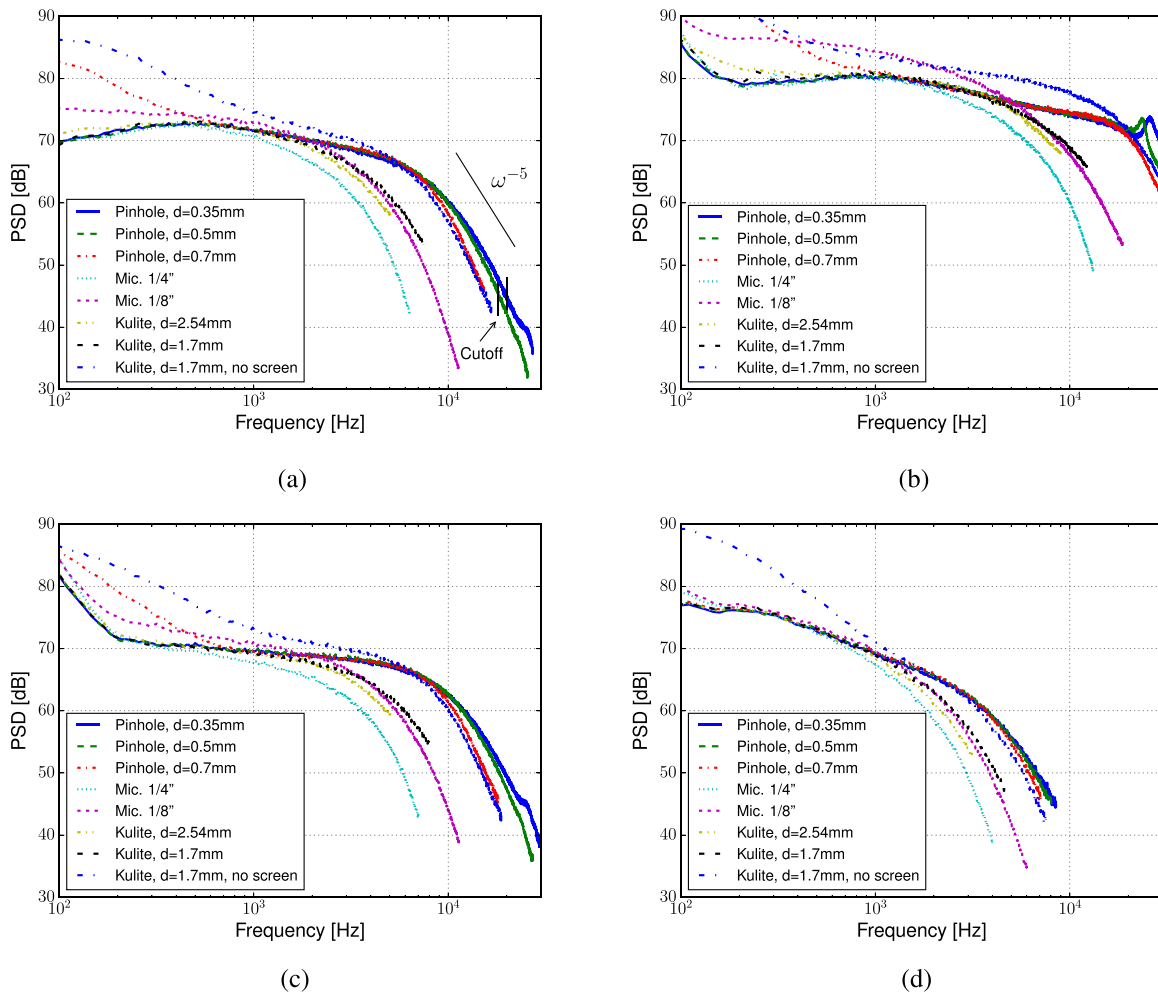


**FIG. 6.** Corrected spectra, (a) ZPG, $U_\infty = 30$ m/s; (b) ZPG, $U_\infty = 60$ m/s; (c) FPG-12°, $U_\infty = 30$ m/s; (d) APG 12°, $U_\infty = 30$ m/s.

ZPG and FPG cases with $U_\infty = 30$ m/s and $d^+ > 18$, a small attenuation may be expected in the remaining $\omega^{-5}$ region. This uncertainty in the reference spectra may affect the resulting attenuation value for the pinhole-mounted sensors but not for the flush-mounted sensors. In the latter case, the corrected spectra are limited to frequencies below the $\omega^{-5}$ region. Note that the flush-mounted Kulite sensor without screen is not considered any further due to the strong spectral disturbances present for all measured flow conditions.

Figure 7 shows the obtained spectral attenuation for different sensors. Apart from the low-frequency disturbances, the attenuation is negligible at low frequencies (below 1 kHz) except for the 1/4-in. microphone case. The attenuation increases with increasing frequency. The increase is more pronounced at high frequencies and for sensors with a larger sensing area. For example, for the 1/4-in. microphone in ZPG with $U_\infty = 30$ m/s, the attenuation is visible starting from 500 Hz and increases up to 4 dB at 2 kHz. From 2 to 6 kHz, the attenuation increases rapidly and reaches 20 dB. As expected, the attenuation spectra are shifted toward higher frequencies at a larger velocity, see Figs. 7(a) and 7(b). For the APG and FPG cases, the attenuation

spectra have a similar spectral shape to that in ZPG. However, the attenuation begins at a lower frequency in APG, which can significantly affect the attenuation level at high frequencies. For example, the attenuation at 4 kHz measured with the 1/4-in. microphone increases from 10 dB in ZPG up to 20 dB in APG. For FPG, no corresponding trends can be observed.

### C. Corcos correction

The unsteady pressure measured by a sensor is given by[1]

$$p_m(\boldsymbol{x}, t) = \int_\infty p(\boldsymbol{s}, t) K(\boldsymbol{s} - \boldsymbol{x})\, dA(\boldsymbol{s}), \qquad (2)$$

where $\boldsymbol{x}$ is the position of some reference point on the sensor surface and the response kernel $K$ represents the contribution to the sensor's output signal caused by a pressure at $\boldsymbol{s}$. If the unsteady pressure field is statistically stationary and homogeneous over the sensor surface, which holds for most practical applications, the measured pressure one-point spectrum can be determined by
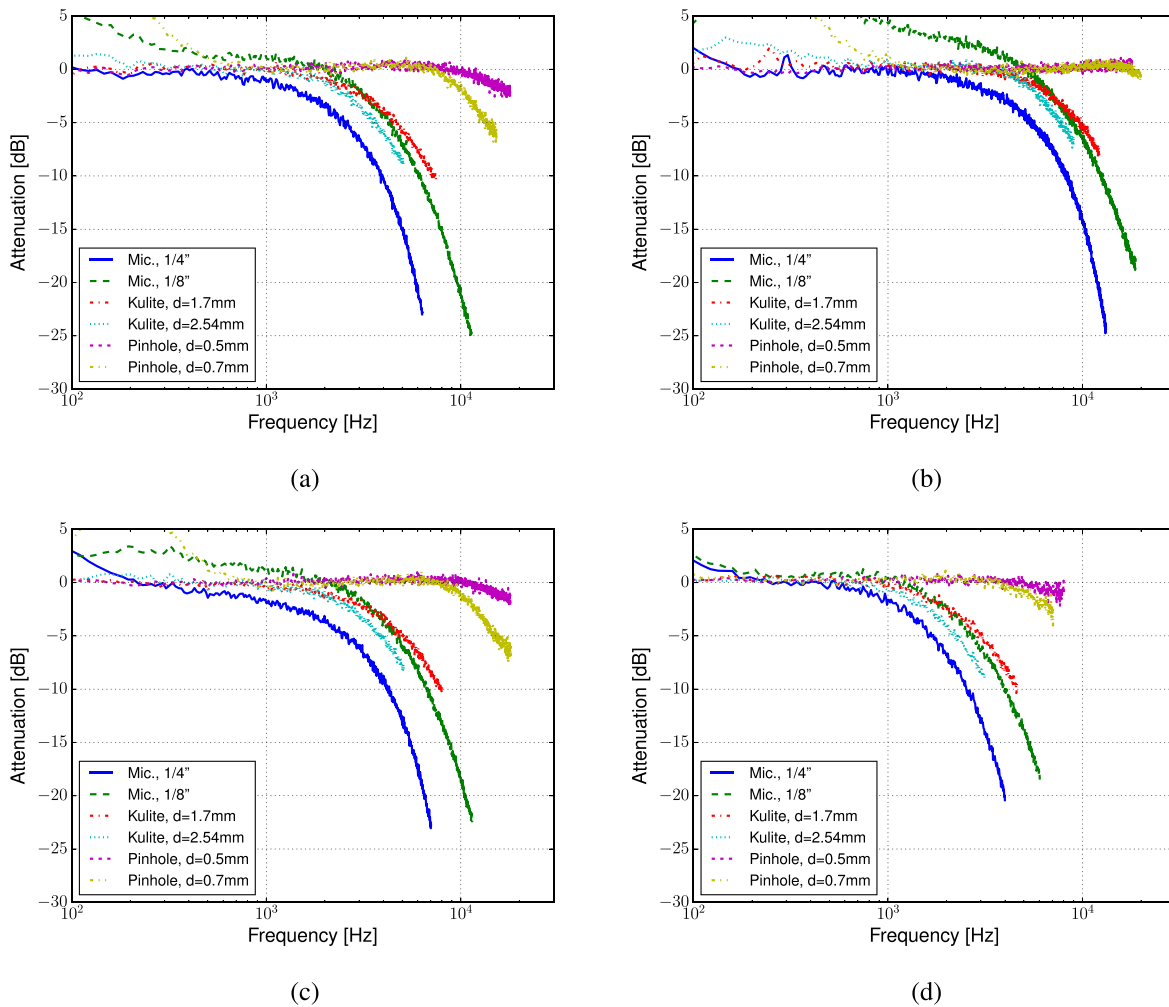


(a)



(b)



(c)



(d)

**FIG. 7.** Attenuation spectra, (a) ZPG, $U_\infty = 30$ m/s; (b) ZPG, $U_\infty = 60$ m/s; (c) FPG -12°, $U_\infty = 30$ m/s; (d) APG 12°, $U_\infty = 30$ m/s.

$$\Phi_m(\omega) = \int_\infty \int_\infty \Phi(\omega) \Gamma(\boldsymbol{\varepsilon}, \omega) K(\boldsymbol{s}) K(\boldsymbol{s} + \boldsymbol{\varepsilon}) \, dA(\boldsymbol{s}) \, dA(\boldsymbol{\varepsilon}), \quad (3)$$

where $\Phi(\omega)$ is the actual one-point pressure spectrum and $\Gamma(\boldsymbol{\varepsilon}, \omega)$ is the pressure coherence spectrum for two points with a separation of $\boldsymbol{\varepsilon}$. Hence, the spectral attenuation can be calculated with

$$\frac{\Phi_m(\omega)}{\Phi(\omega)} = \int_\infty \Gamma(\boldsymbol{\varepsilon}, \omega) \Theta(\boldsymbol{\varepsilon}) \, dA(\boldsymbol{\varepsilon}), \quad (4)$$

where

$$\Theta(\boldsymbol{\varepsilon}) = \int_\infty K(\boldsymbol{s}) K(\boldsymbol{s} + \boldsymbol{\varepsilon}) \, dA(\boldsymbol{s}) \quad (5)$$

is a function exclusively determined by the sensor characteristics.

Corcos[1] determined the measured spectral attenuation by solving Eq. (4). The functions $\Theta(\boldsymbol{\varepsilon})$ and $\Gamma(\boldsymbol{\varepsilon}, \omega)$ in this integral equation were estimated as follows:

A uniform sensitivity over the sensor surface was assumed to determine $\Theta(\boldsymbol{\varepsilon})$, that is, $K(\boldsymbol{s}) = 1/\sigma$ for $\boldsymbol{s}$ inside the sensor surface and $K(\boldsymbol{s}) = 0$ otherwise. Here, $\sigma$ denotes the surface area of the sensor and for a circular sensor $\sigma = \pi r^2$. In this paper, the focus is on sensors with a circular sensing surface, which are also of the most practical interest.

With the uniform sensitivity assumption, the function $\Theta(\boldsymbol{\varepsilon})$ becomes a function for the overlapping area of two circles separated by $|\boldsymbol{\varepsilon}|$, expressed as

$$\Theta(\boldsymbol{\varepsilon}) = \frac{2}{\pi^2 r^2} \left[ \cos^{-1}\left(\frac{|\boldsymbol{\varepsilon}|}{2r}\right) - \frac{|\boldsymbol{\varepsilon}|}{2r} \sqrt{1 - \left(\frac{|\boldsymbol{\varepsilon}|}{2r}\right)^2} \right]. \quad (6)$$

To estimate the coherence spectrum $\Gamma(\boldsymbol{\varepsilon}, \omega)$, an expression with a separable form was suggested,

$$\Gamma(\boldsymbol{\varepsilon}, \omega) = A(\omega\varepsilon_x/U_c) B(\omega\varepsilon_z/U_c) \exp(-i\omega\varepsilon_x/U_c), \quad (7)$$

where $\boldsymbol{\varepsilon} = (\varepsilon_x, \varepsilon_z)$ and $U_c$ is the convection velocity of the surface pressure field. The functions $A$ and $B$ represent the coherence decay in

the streamwise and spanwise directions, respectively. The exponential function provides the phase differences caused by the convection of the pressure field between two points with $\varepsilon_x$ apart. The form of the functions $A$ and $B$ was determined by fitting the measurement results of Willmarth and Wooldridge.[31]

The spectral attenuation was calculated by Corcos[1] using Eq. (4) with the help of Eqs. (6) and (7). The results were given at discrete frequencies between $0.05 \le \omega r/U_c \le 10$, shown in Fig. 8. In a later study, Corcos[32] proposed a semi-empirical model representing the coherence of the pressure field

$$\Gamma(\boldsymbol{\varepsilon}, \omega) = \exp(-\alpha\omega\varepsilon_x/U_c) \exp(-\beta\omega\varepsilon_z/U_c) \exp(-i\omega\varepsilon_x/U_c). \quad (8)$$

The functions $A$ and $B$ in Eq. (7) are formulated with two exponential functions in Eq. (8). The value of these functions is governed by the coefficients $\alpha$ and $\beta$, which can be empirically determined. The coefficient values of $\alpha = 0.11$ and $\beta = 0.73$ based on the measurement result of Willmarth and Wooldridge.[31] With these values, Eq. (8) can be applied instead of Eq. (7). The calculated attenuation spectrum is shown in Fig. 8(a), which is consistent with the attenuation values provided by Corcos.[1]

There is no doubt that the streamwise and spanwise coherence can be well described with the exponential functions.[7,8] However, for the prediction of the off-axis coherence, the applied form had no proof and only limited publications have reported the off-axis coherence. Smol'yakov and Tkachenko[33] proposed a different model based on a wind tunnel's measurement dataset, which reads

$$\Gamma(\boldsymbol{\varepsilon}, \omega) = \exp\left(-\sqrt{(\alpha\omega\varepsilon_x/U_c)^2 + (\beta\omega\varepsilon_z/U_c)^2}\right) \exp(-i\omega\varepsilon_x/U_c). \quad (9)$$

This model has the same expression as the Corcos[32] model when considering the streamwise or spanwise coherence only, that is, $\varepsilon_x = 0$ or $\varepsilon_z = 0$. The difference between both models is that Smol'yakov and Tkachenko[33] used an elliptical combination for calculating the off-axis coherence. In more recent studies, the measurements from Leclercq and Bohineust[34] and Hu[35] showed that the Corcos model underpredicts
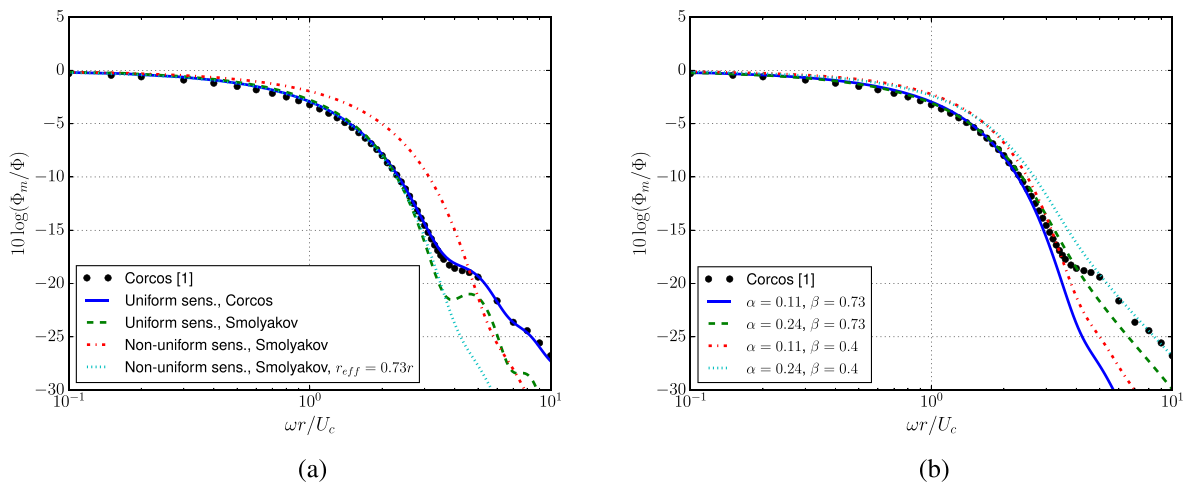


**FIG. 8.** Theoretical prediction of the attenuation spectra, (a) ZPG; and (b) APG.

the off-axis coherence. Furthermore, the off-axis coherence can be well predicted by the Smol'yakov and Tkachenko model in both spatial and frequency domains, and also with pressure gradients.[35]

Hence, the attenuation is calculated with the Smol'yakov and Tkachenko[33] model, using Eq. (9) instead of Eq. (8). The result shows that there is almost no difference in the predictions at low frequencies $\omega r/U_c < 2.5$ between using the two models, see Fig. 8(a). However, at higher frequencies the attenuation calculated using the Smol'yakov and Tkachenko model drops more rapidly and the difference between both predictions becomes larger. This may be because, first, the difference of the off-axis coherence prediction between Eqs. (8) and (9) is small at low $\omega r/U_c$ and becomes larger with increasing frequency. Second, at a larger $\omega r/U_c$, the attenuation is significantly increased due to the phase cancelation. A pressure field predicted by the Smol'yakov and Tkachenko model with a larger off-axis coherence may effectively increase the phase cancelation and cause a larger attenuation correspondingly.

According to Eq. (4), an accurate representation of $\Theta(\varepsilon)$ is also important for calculating the attenuation. Apparently, the assumption of uniform sensitivity, which leads to Eq. (6), does not correspond to the reality. The sensitivity over an actual sensor surface is largest at the center area and falls down to zero toward the edge. Based on a measurement on a condenser microphone,[15] Blake[36] suggested the response kernel for $|s| \leq r$ as a function of the sensor radius, expressed as

$$K(s) = 0.198\,[1 + 4.06 J_0(2.96\,|s|/r)]/(K\,\sigma), \tag{10}$$

where $J_0$ is the zero-order Bessel function of the first kind and $K = \int K(s)\,dA(s)$ is the calibration factor ensuring the integration of $K(s)$ over the sensor surface equal to unity. With the above expression for $K(s)$, the effect of non-uniform sensitivity can be taken into account by introducing an effective radius of the sensor. Gilchrist and Strawderman[12] assumed an effective response kernel with a constant sensitivity over a smaller area that leads to the effective radius being equal to the root mean square of the function $K(s)$. White[13] argued that the coherence $\Gamma(\varepsilon, \omega)$ of the wall pressure field needs to be considered when investigating the effect of non-uniform sensitivity on the signal output. The function $\Theta(\varepsilon)$ can be evaluated with the help of Eq. (5) together with $K(s)$, which uses the non-uniform sensitivity distribution.

Following White's[13] concept, the spectral attenuation is calculated taking into account the effect of non-uniform sensitivity [see Fig. 8(a)]. It results in a smaller attenuation compared to the one calculated with uniform sensitivity, as a result of the smaller effective area. By applying a factor of 0.73 to the sensor radius, that is, $r_{eff} = 0.73\,r$, the spectrum collapses with the one calculated with uniform sensitivity at $\omega r/U_c < 3.5$. The frequency shift and the obtained factor for the effective radius are consistent with the findings of Ref. 13, where a slightly smaller factor of approximately 0.7 was given. This difference is probably due to different formulations of the applied function $K(s)$. Surprisingly, the conspicuous kinks at frequencies $\omega r/U_c > 3.5$ calculated with uniform sensitivity are smoothed out by using non-uniform sensitivity. It is worth mentioning that viscous damping becomes important for the membrane displacement at high frequencies, which could have a significant influence on $K(s)$, affecting the attenuation results.[15]

According to investigations of the pressure-gradient effect on the wall pressure coherence,[8,17,35] the coherence is significantly affected by an APG, which increases the streamwise coherence decay and slows

down the spanwise decay. To illustrate the APG effect on the attenuation, $\alpha = 0.24$ and $\beta = 0.4$ are applied in Eq. (9), which represent the wall pressure coherence in a strong APG.[35] Figure 8(b) shows that the APG decreases the attenuation level against the non-dimensional frequency, $\omega r/U_c$. The values of $\alpha$ and $\beta$ are also changed separately from the values in ZPG to evaluate the APG effect in each direction. The result shows that the increased spanwise coherence leads to a broadband reduction in the attenuation level, as expected according to Eq. (4). There is almost no increase (only minimal at $\omega r/U_c < 1.5$) in the attenuation level observed due to the reduced streamwise coherence. However, the reduced coherence causes a significant decrease in the attenuation level at frequencies $\omega r/U_c > 3$. This may be related to a weakened phase cancelation due to the less correlated pressure field in the streamwise direction.

### D. Scaling of the attenuation spectra

In this section, the attenuation spectra are scaled with $r/U_c$ as suggested by Corcos.[1] For this scaling, $r$ represents the radius of the effective sensing area, which, for example, is significantly smaller than the geometric sensor size when the non-uniform sensitivity is taken into account. The variable $U_c$ represents the convection velocity, which needs to be determined separately for sensors with different sizes or configurations.

The 1/4-in. microphone is taken as a reference for the investigation of the spectra scaling. This choice is made for the following reasons. First, no noticeable disturbances of the spectra measured by the 1/4-in. microphone were observed. Second, the effective sensing area of the microphone membrane can be precisely defined based on the knowledge gained in Sec. III C. Finally, the convection velocity needed for the scaling is frequency and distance dependent, which can be determined with $U_c(\Delta x, \omega) = \Delta x\,\omega/\theta(\Delta x, \omega)$, where $\theta(\Delta x, \omega)$ is the phase difference between two sensors with $\Delta x$ apart. The convection velocity with the smallest sensor separation of $\Delta x = 2$ mm (located at $x = 1170$ and 1172 mm, see Fig. 2) is used for the scaling. This value may provide a satisfactory approximation of the "averaged" convection velocity over the sensor surface because the distance of 2 mm is close to the active membrane radius ($r = 2.15$ mm) of the 1/4-in. microphone.

Figure 9(a) shows the obtained convection velocity with $\Delta x = 2$ mm for all test cases listed in Table I, along with the fitting curves according to

$$U_c/U_e = \frac{a_1\,\omega\delta^*/U_e}{1 + b_1\,(\omega\delta^*/U_e)^{2.5}} + c_1. \tag{11}$$

where $a_1$, $b_1$, and $c_1$ are the parameters, which need to be determined by fitting the measured convection velocities. The above expression is suggested based on the Smol'yakov model,[37] which reads

$$U_c/U_e = \frac{a_1\,\omega\delta^*/U_e}{1 + b_1\,(\omega\delta^*/U_e)^{2}} + c_1. \tag{12}$$

There is a slight difference in the power value of $\omega\delta^*/U_e$ in the denominator between the two expressions. This power value affects the peak position and the mid-frequency spectral shape. After testing different values with a step change of 0.5, the value of 2.5 provides the best fit for the present dataset. An example of the curve fitting for a ZPG case and an APG case using Eqs. (11) and (12) is shown in Fig. 9(b). For the ZPG case, both expressions achieve good predictions with similar results.
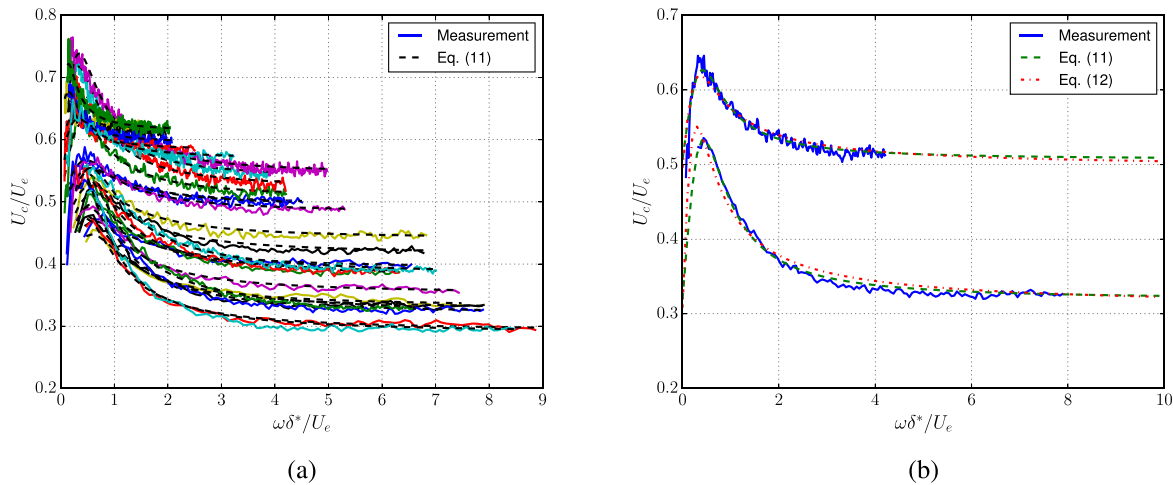
**FIG. 9.** Curve fitting of the convection velocity, (a) all the test cases listed in Table I; (b) ZPG (larger values) and APG 12° (smaller values) with $U_\infty = 30$ m/s.

However, for the APG case, a better prediction obtained with Eq. (11) can be observed. Note that the pressure gradient affects the magnitude of $U_c$, and particularly, the magnitude decreases significantly in APG. For a given frequency, the reduced $U_c$ increases $\omega r/U_c$, leading to a larger attenuation [see Figs. 7(a) and 7(d)].

Figure 10 shows the scaled attenuation spectra measured by the 1/4-in. microphone for all test cases. The effective radius $r$ and the fitting curves of $U_c$ [see Fig. 9(a)] are applied for the scaling. The effective radius is estimated based on the discussion in Sec. III C, i.e., $r = 0.73\, r_{membrane}$ with $r_{membrane} = 2.15$ mm. The Corcos correction[1] and the result calculated using the non-uniform sensitivity distribution are also plotted for a reference.

The results show that the scaled attenuation spectra collapse for the ZPG and FPG cases and have excellent agreement with the theoretical prediction. For the APG case, the spectra are shifted to higher frequencies, which agree with the theoretical calculation, as illustrated in Fig. 8(b). Compared to the Corcos[1] correction, the prediction range with high precision is increased to $\omega r/U_c \simeq 3.5$ with a magnitude of 23 dB, by taking the non-uniform sensitivity into account and using the Smol'yakov and Tkachenko[33] model. At frequencies $\omega r/U_c > 3.5$, the calculated attenuation deviates from the exponential growth and increases slower. This high-frequency development cannot be verified or refuted due to the limitation of the frequency range of the measured attenuation spectra. However, from the measurement result, there is no evidence of a deviation from the exponential growth up to 25 dB [see Fig. 10(a)]. Note that the effect of the membrane damping on the sensitivity distribution is not considered in the theoretical calculation which could affect the predicted result, especially at high frequencies.

To scale the attenuation spectra measured by the other sensors, the effective radius and the corresponding convection velocity for each sensor need to be determined. There are three types of sensors or sensor configurations considered, that is, flush-mounted 1/8-in. microphone without screen, flush-mounted Kulite sensors with B-screen, and the pinhole-mounted Kulite sensors.

For the flush-mounted 1/8-in. microphone, the effective radius can be determined in the same way as for the 1/4-in. microphone, that is, $r = 0.73\, r_{membrane}$ with the active radius of $r_{membrane} = 1.05$ mm.

However, for the other sensors, the effective radius cannot be calculated in the same way because the wall pressure fluctuations do not act directly on the sensing surface. For example, for the flush-mounted Kulite sensor, the signal of the wall pressure fluctuations goes through the miniholes placed in a circle on the screen and then is averaged on the sensing chip. The distance between the miniholes may be more important for the signal averaging than the chip size. This is because the coherence and phase difference of the pressure fluctuations acting on the chip are mostly determined by the distribution of the miniholes. Thus, the distance between the center of the screen and the minihole is taken as the radius for the scaling, that is, $r = 0.6$ and 0.875 mm for the Kulite sensors with $d = 1.7$ and 2.54 mm, respectively. For the pinhole-mounted sensors, the radius of the pinhole is used for the scaling.

The convection velocity needs to be determined separately for each sensor due to the convection distance dependence of $U_c$. However, the value of $U_c$ for small separations ($\Delta x < 2$ mm), which correspond to the sensor size, cannot be measured. The value is estimated based on the measured results of $U_c$ for separations at $\Delta x \geq 2$ mm (see Appendix B). Figure 21(a) shows that the magnitude of $U_c$ increases with a larger separation. The spectral shapes of $U_c$ remain similar with different separations, and the spectra collapse when applying a distance-dependent scaling factor. If it is assumed that the spectral shape of $U_c$ at smaller separations is comparable with that for the larger separations, $U_c(\omega, \Delta x < 2$ mm$)$ can be estimated using $U_c(\omega, \Delta x = 2$ mm$)$ with a scaling factor. The scaling factor $\tau_u$ used for each sensor is determined by fitting the attenuation spectra to that of the 1/4-in. microphone. The obtained scaling factors, shown in Fig. 21(d), are $\tau_u = 0.79$ for the 1/8-in. microphone and the Kulite sensor with $d = 2.54$ mm, and $\tau_u = 0.73$ for the Kulite sensor with $d = 1.7$ mm. For the pinhole-mounted sensors, $\tau_u = 0.7$ is applied to all pinhole sizes because the velocity is assumed to approach a constant value at very small separations, as well as for the large separations.

Figure 11 shows the scaled attenuation spectra for the cases considered in Fig. 6, based on the estimated values of $r$ and $U_c$. For the flush-mounted sensors, a good match is observed for the APG case and at high frequencies $\omega r/U_c > 1.5$ for all the other cases. A clear disturbance at low and medium frequencies is visible for the spectrum
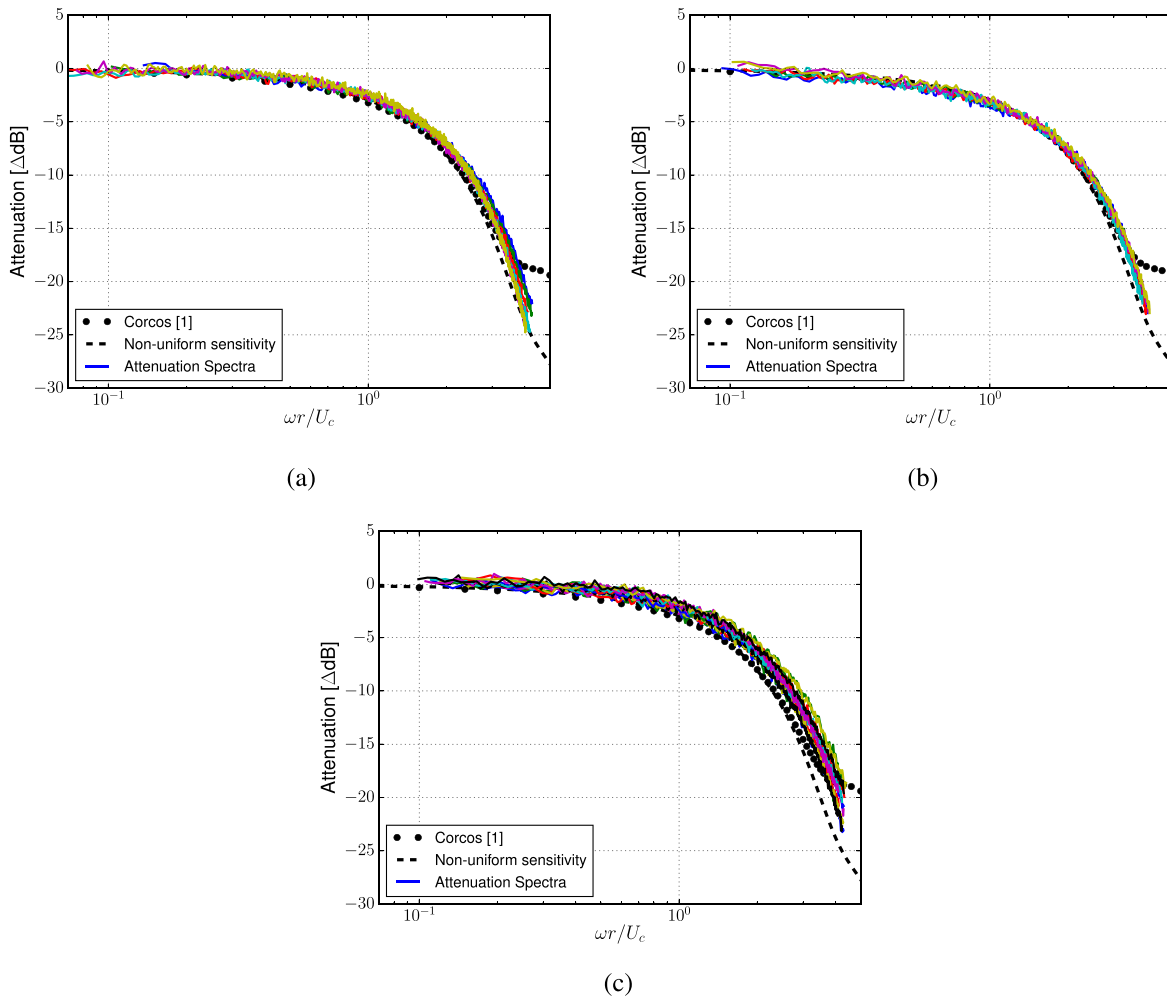
(a)



(b)



(c)

**FIG. 10.** Spectral attenuation for the flush-mounted 1/4″ microphone, (a) ZPG; (b) FPG; and (c) APG.

measured by the 1/8-in. microphone. This is caused by the sensor installation-related issues discussed in Sec. III B. Furthermore, these issues may cause small disturbances at medium frequencies as reported in Ref. 18, leading to discrepancies in the spectra for the case with a higher velocity of $U_\infty = 60$ m/s and with FPG.

For the pinhole-mounted sensors, the attenuation is much smaller than that for the flush-mounted sensors. Noticeable attenuation is observed at a much higher frequency at $\omega r/U_c > 1.3$ for all the measured cases and the magnitude is smaller than 2 dB at $\omega r/U_c = 2$, whereas it reaches 7–8 dB for the flush-mounted sensors. Note that the attenuation spectra measured by both pinhole-mounted sensors do not correspond to each other, indicating some add-on effect due to the different pinhole sizes.

### E. Modeling of the attenuation spectra

Based on the good match of the scaled attenuation spectra for the flush-mounted sensors, an empirical correction model for the attenuation spectra can be developed with the application of appropriate

$r$ and $U_c$. A correction for the pinhole-mounted sensors is not considered because their attenuation spectra do not correspond to each other.

To model the correction, the attenuation spectra measured by the 1/4-in. microphone are used as reference due to the large useful frequency range. Figure 12 shows examples of an excellent fit to the attenuation spectra for a ZPG case and an APG case using a power-function expression

$$10 \log \left( \frac{\Phi_m(\omega)}{\Phi(\omega)} \right) = a_2 \left( \frac{\omega r}{U_c} \right)^{b_2},\tag{13}$$

where $a_2$ is an amplitude factor and $b_2$ controls the spectral shape. Furthermore, both variables are assumed to be boundary-layer-parameter dependent. Using Eq. (13) to fit the measured spectra of all test cases listed in Table I, the values of $a_2$ and $b_2$ are determined and plotted in Fig. 13. The results illustrate the dependence of $a_2$ and $b_2$ on the selected TBL parameters $u_\tau/U_e$ and $Re_\tau$, respectively, and the best fit curves are found as
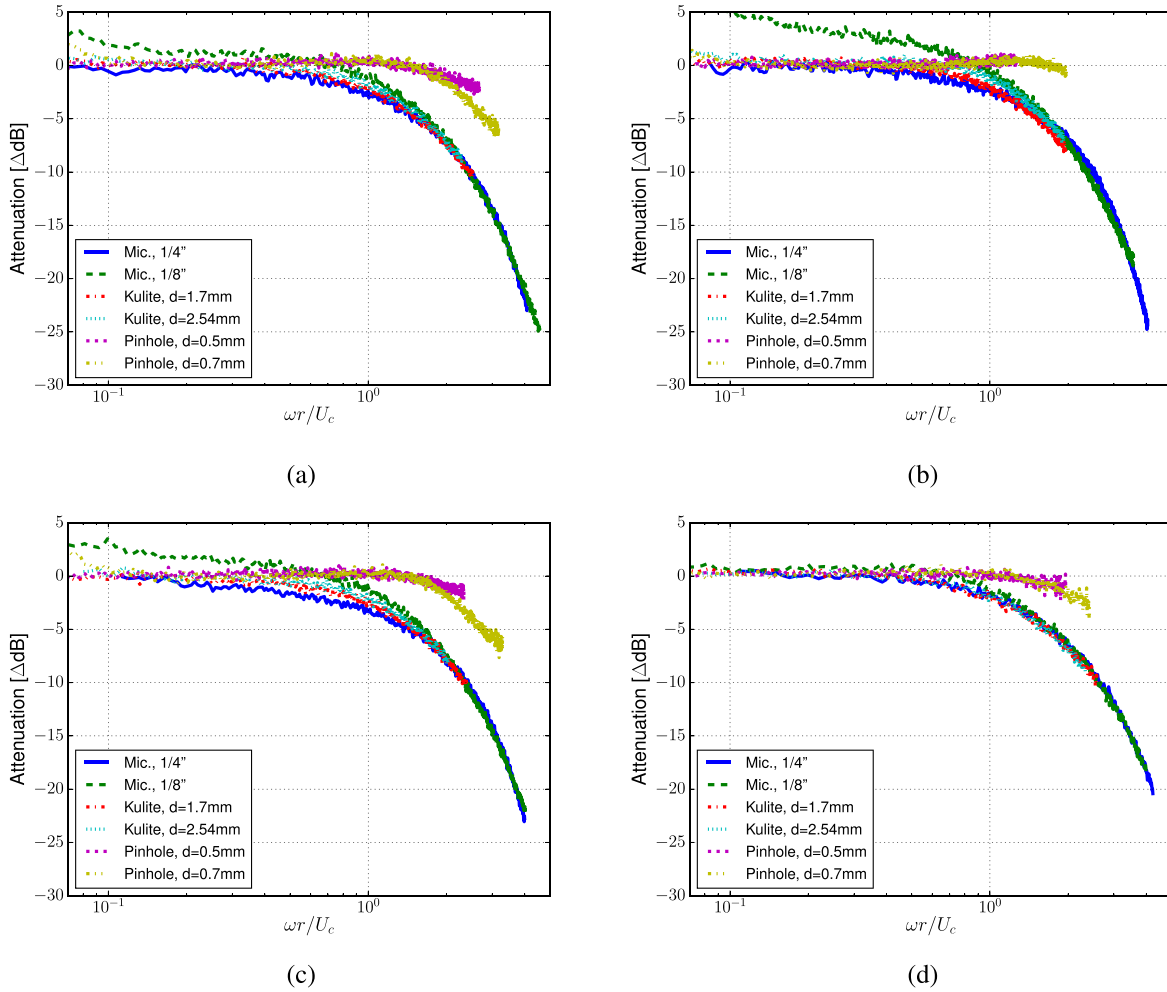
**FIG. 11.** Scaled attenuation spectra, (a) ZPG, $U_\infty = 30$ m/s; (b) ZPG, $U_\infty = 60$ m/s; (c) FPG-12°, $U_\infty = 30$ m/s; and (d) APG 12°, $U_\infty = 30$ m/s.

$$a_2 = -32.505 \, u_\tau/U_e - 1.275, \qquad (14)$$

$$b_2 = 0.704 \, Re_\tau^{0.112}. \qquad (15)$$

To apply the correction, the values of $r$ and $U_c$ need to be determined according to individual test conditions. Regarding the sensor effective radius $r$, the present measurement covers a large range of sensor types, which are commonly applied for the wall-pressure fluctuation measurement. The values used in this work are recommended for general use, and the criteria for determining the effective radius can be used for other sensor types not covered in this work.

For the application of $U_c$ with individual sensor types, the value can be estimated using $U_c(\omega, \Delta x = 2$ mm) with a scaling factor, which is used in this work or can be estimated for other sensor types according to the result shown in Fig. 21(d). However, $U_c$ at $\Delta x = 2$ mm still needs to be modeled, which is done by fitting the measurement results with Eq. (11) (see Fig. 9(a). The determined values of the variables are shown in Fig. 14, along with the best-fit curves according to

$$a_1 = \max((1.157 \, Re_\tau - 793)/Re_\tau, 0.1), \qquad (16)$$

$$a_1/b_1 = \max((0.164 \, Re_\theta - 300)/Re_\theta, 0.01), \qquad (17)$$

$$c_1 = 0.973 \, H^{-1.748}. \qquad (18)$$

In the expression for $U_c$ in Eq. (11), the variables $a_1$ and $b_1$ affect the peak level and the spectral shape at low and medium frequencies. An increase in $a_1$ or a decrease in $b_1$ would raise the peak level, and vice versa. By investigating the dependence between the above variables and TBL parameters, it can be said that both variables are mainly dependent on the Reynolds number. The limits applied in Eqs. (16) and (17) avoid that the peak level is too large or too small (no peaks), leading to unexpected results. Note that, due to the low-frequency disturbance, the peaks cannot be clearly identified in some test cases [see Fig. 9(a)]. Those cases are not taken into account for the determination of the variables. Furthermore, the relation for the variable $b_1$ on the TBL parameter is expressed as $a_1/b_1$ due to the better fitting result. This may be because the peak level and the spectral shape at medium
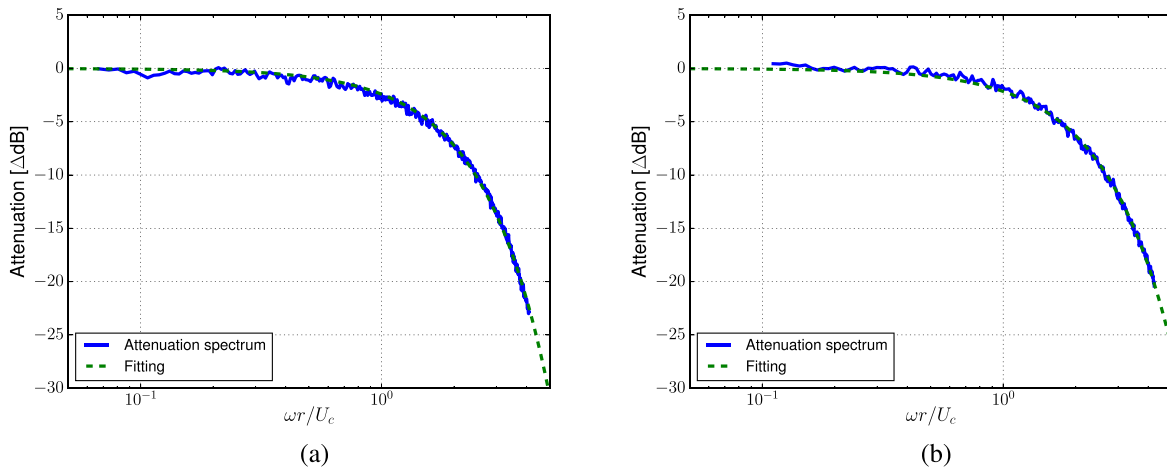
**FIG. 12.** Curve fitting of the attenuation spectra with $U_\infty = 30$ m/s according to Eq. (13), (a) ZPG; and (b) APG 12°.

frequencies are affected by $a_1/b_1$ rather than $b_1$. The variable $c_1$ controls the high-frequency magnitude, which can be significantly affected by the pressure gradient. Based on the experience with the wall pressure spectra modeling,[38,39] the Clauser parameter $\beta_{\delta^*}$ and the boundary layer shape factor $H$ could be the good candidates for predicting the pressure gradient effect. The disadvantage of using $\beta_{\delta^*}$ is that the value of $\beta_{\delta^*}$ is strongly affected by the local pressure gradient. This may weaken the importance of the near-upstream history. However, the near-upstream history is assumed to be important for the wall pressure fluctuations due to the lag effects of pressure gradients.[8,18,40] The TBL flow with a local ZPG, that is, $\beta_{\delta^*} = 0$, but which experiences a near-upstream pressure gradient may have similar wall pressure spectra as that in pressure gradient flows.[18] Instead, the parameter $H$ is mainly affected by the flow history. Therefore, it is selected and the result shows that the value of $c_1$ can be well predicted using Eq. (18).

### F. Application of the correction model

To assess the generality of the proposed correction, four other test cases are selected. These are three experiments conducted in other facilities and one conducted in the present measurement setup but using a different sensor. The wall pressure spectra of the experiments conducted in other facilities were measured at different fuselage positions of an Advanced Technology Research Aircraft Airbus A320 in flight tests,[41] at $x/c = 0.99$ ($c$ denotes the chord length) on the suction side of a NACA 0012 airfoil with different AOAs in wind tunnel tests,[42] and at a rear roof section of a Mercedes-Benz E-Class model in wind tunnel tests.[43] The TBL parameters of those cases needed for the application of the correction are listed in Table II. The parameters for the aircraft and airfoil tests were obtained by CFD calculations[44,45] and for the car test were measured using a pitot tube rake. Note, that for the airfoil test cases, the numerical results are used instead of the
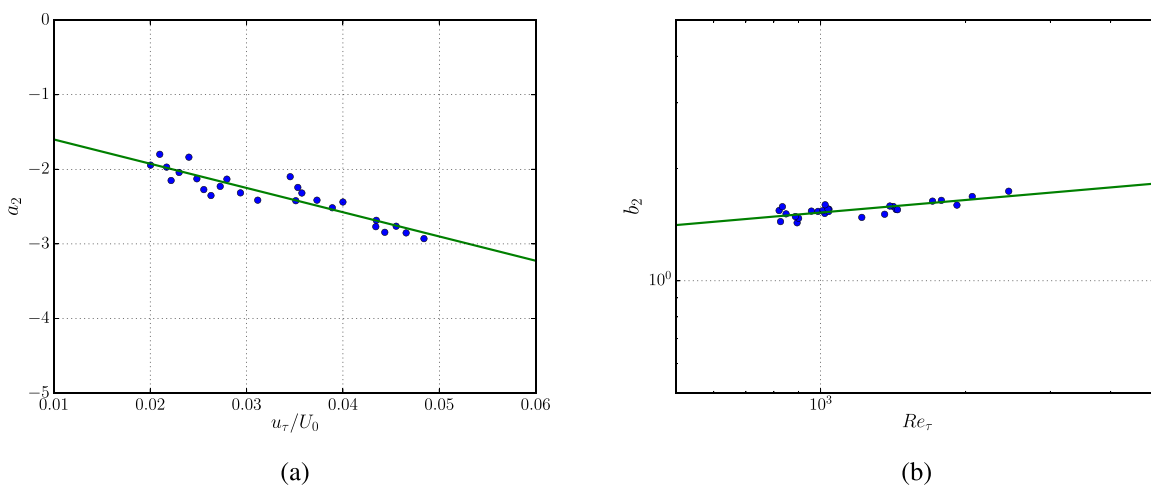


**FIG. 13.** Determination for variables in Eq. (13) and curve fitting according to Eqs. (14) and (15), (a) $a_2$; and (b) $b_2$.
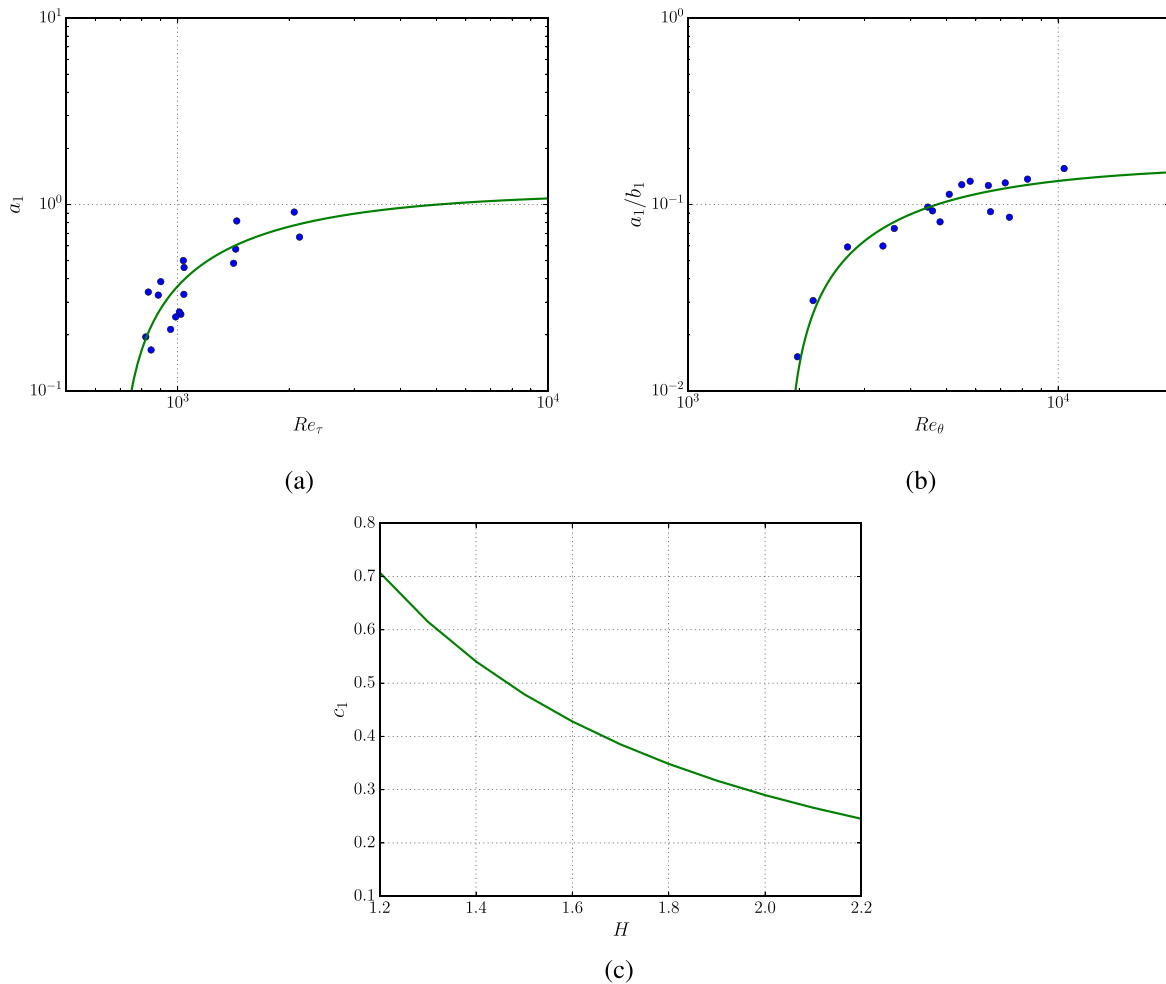
**FIG. 14.** Determination for variables in Eq. (11) and curve fitting according to Eqs. (16)–(18), (a) $a_1$; (b) $a_1/b_1$; and (c) $c_1$.

measurement results. This is because the TBL parameters were measured at the position slightly behind the trailing edge ($x/c = 1.0038$), which could have a more than 10% larger TBL thickness compared to that at $x/c = 0.99$, reported in Ref. 46. Furthermore, the value of $H$ for the flight test cases is calculated based on incompressible flow assumption, that is, without taking variations in air density into account. The following considerations are behind this choice: the TBL velocity profile that can be represented by the parameter $H$ is assumed to be an important factor in determining the wall-pressure convection velocity $U_c$. If the air density variation within the compressible TBL flow is considered, the value of $H$ will increase significantly. For example, for the aircraft's front position case, the value increases up to 1.67 instead of 1.34, although with a ZPG-like velocity profile.[44] The increased value can significantly lower the predicted magnitude of $U_c$ according to Eqs. (11) and (18), which is unexpected based on the measured convection velocity from the flight tests.[44]

Before applying the correction, we need to determine the values of $r$ and $U_c$ for each selected case. For the one conducted in the present measurement setup, the wall pressure spectra were measured with a surface microphone GRAS 48LA, which has an active membrane radius of $r = 1.8$ mm. For the flight test cases, surface microphones B&K 4948 with an active membrane radius of $r = 4.5$ mm were applied. For both microphones, the factor of 0.73 derived previously can be applied for the calculation of the effective radius, that is, $r_{eff} = 0.73\, r$. The values of $U_c$ for the GRAS and B&K microphones are estimated based on the development of the scaling factor $\tau_u$ according to the microphone radius, resulting in $U_c = 0.96\, U_c(\omega, \Delta x = 2$ mm) and $U_c = 1.12\, U_c(\omega, \Delta x = 2$ mm), respectively [see Fig. 21(d)]. For the airfoil and car test cases, the Kulite LQ-062 and XT-140M (the same as the present test) with B-screens were applied, respectively. The values of $r$ and $U_c$ used for the Kulite sensors in the present test are taken. Note that the Kulite LQ-062 has a slightly smaller sensor radius ($r = 0.8$ mm) than the Kulite XCQ-062 ($r = 0.85$ mm) used in the present test, but with the same B-screen configuration (same distances between mini-holes), which is assumed to be decisive for determining the effective radius.

Figures 15–18 show the measured and corrected wall pressure spectra. In Fig. 15, the spectra measured with the pinhole-mounted

**TABLE II.** Boundary layer parameters of selected cases.

| | $U_e$ (m/s) | $\delta^*$ (mm) | $H = \delta^*/\theta$ | $u_\tau$ (m/s) | $Re_\tau = u_\tau\delta/\nu$ | $Re_\theta = U_e\theta/\nu$ |
|---|---|---|---|---|---|---|
| Aircraft, front position | 249.9 | 11.41 | 1.34 | 7.19 | 10 162 | 41 448 |
| Aircraft, mid-position | 241.4 | 21.32 | 1.24 | 7.21 | 24 334 | 79 259 |
| Aircraft, rear position | 237.5 | 31.97 | 1.26 | 6.89 | 32 155 | 118 980 |
| NACA 0012, AOA = 0° | 52.3 | 2.52 | 1.69 | 1.19 | 778 | 4964 |
| NACA 0012, AOA = 4° | 51.6 | 3.6 | 1.86 | 0.84 | 672 | 6376 |
| NACA 0012, AOA = 6° | 50.1 | 4.44 | 1.97 | 0.59 | 534 | 7120 |
| NACA 0012, AOA = 0° | 35.4 | 2.73 | 1.73 | 0.78 | 536 | 3563 |
| Car roof, rear section | 44.1 | 8.35 | 1.35 | 1.42 | 5237 | 17 717 |

sensor are included and taken as the actual spectra without attenuation. A cutoff frequency is applied to all the corrected spectra because an over-correction occurs above this frequency. The over-correction is probably due to the sensor-mounting-related disturbance discussed in Sec. III B.

The actual and corrected spectra show great agreement for all three pressure gradient conditions. The correction works well up to the cutoff frequency where a large attenuation occurs. For example, for the ZPG case, an attenuation of more than 20 dB is successfully corrected.
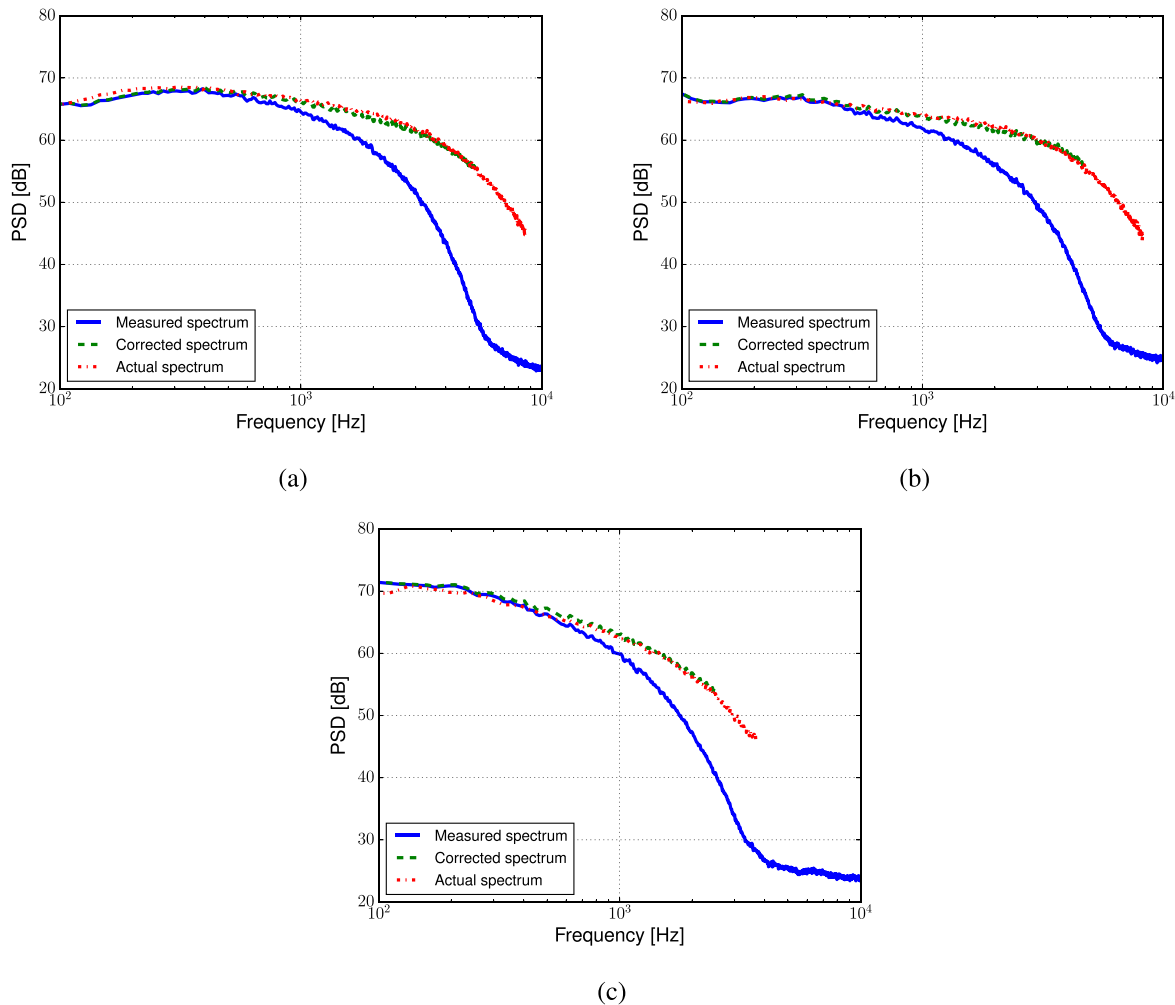


(a)



(b)



(c)

**FIG. 15.** Measured and corrected wall pressure spectra with $U_\infty = 20$ m/s for selected cases listed in Table I, (a) ZPG; (b) FPG II-12°; and (c) APG 12°.
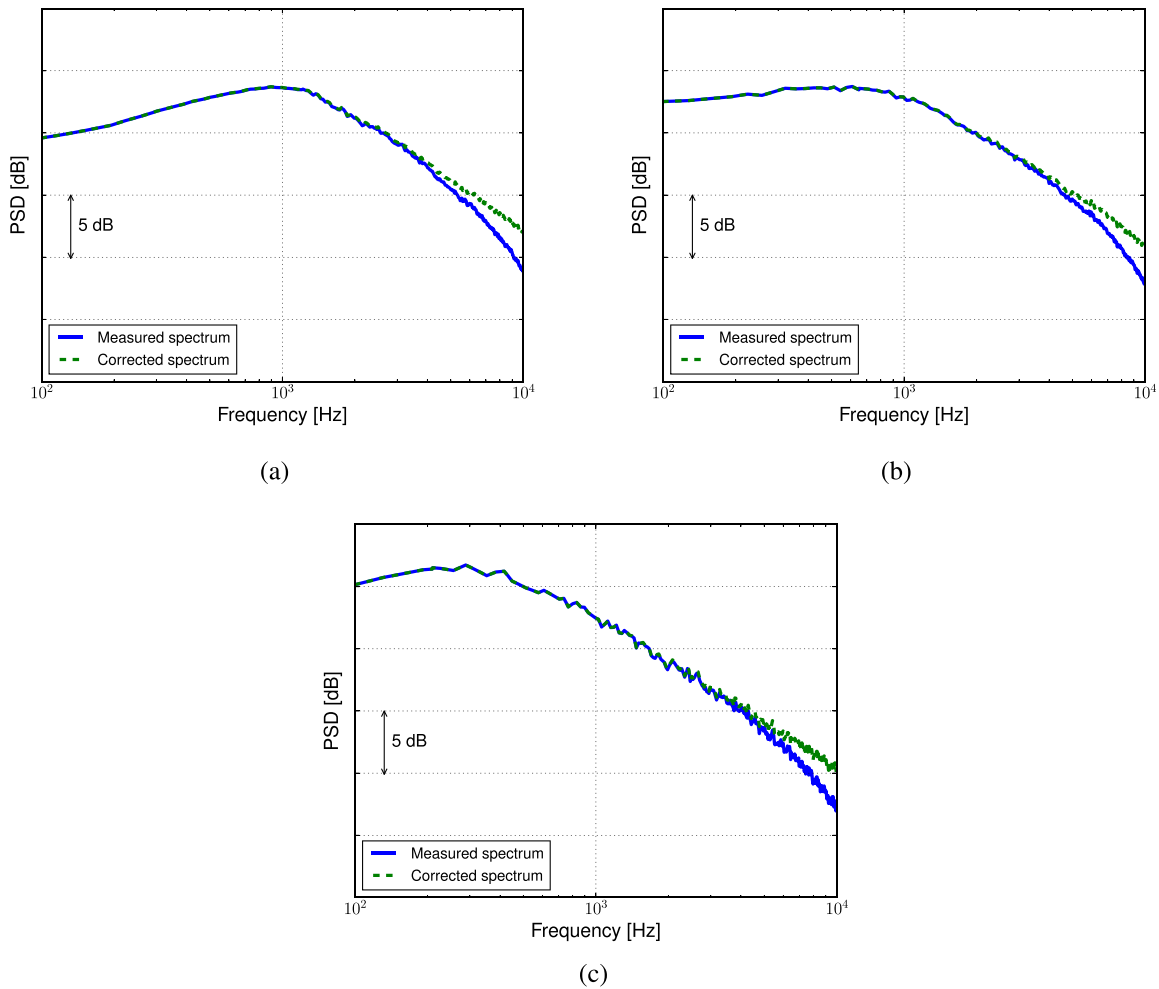
(a)

(b)

(c)

**FIG. 16.** Measured and corrected wall pressure spectra for the flight test cases[41] listed in Table II, (a) front position; (b) mid-position; and (c) rear position.

For the other results shown in Figs. 16–18, the correction works over a wide frequency range and the corrected spectra show a constant slope at medium frequencies as expected for the wall pressure spectra.[17,30,39] However, it is hard to assess the accuracy of the correction because the actual spectra without attenuation are not available. Here, the uncertainty involved in the application of the correction is estimated based on the following two aspects: 1, uncertainty in the variables of the correction model, Eq. (13); 2, uncertainty in the prediction of $U_c$.

Figure 19 shows the effect of the uncertainty in the variables $a_2$, $b_2$, and $U_c$ of Eq. (13) on the corrected spectra, based on the case of ZPG with $U_\infty = 30$ m/s shown in Fig. 12(a). The results show that the effect is small at low frequencies but becomes significant with increasing frequency. For example, a 10% uncertainty in $U_c$ leads to an error of 1 dB at $\omega r/U_c = 2$ and the error increases to 3 dB at $\omega r/U_c = 4$. The effect caused by the uncertainty in variable $a_2$ is small and less relevant than that caused by $b_2$. A 10% uncertainty in $b_2$ can lead to an error of 5 dB at $\omega r/U_c = 4$. Note, that the uncertainty of the fitting curve for the variable $b_2$ [see Fig. 13(b)] is within 5% in all test cases. In general, a large error is not expected due to the uncertainty in the input variables.

## IV. CONCLUSION

A measurement aiming to quantify the wall-pressure-spectra attenuation caused by signal averaging over the sensor surface was conducted in the Acoustic Wind Tunnel Braunschweig (AWB). The turbulent boundary layer (TBL) flow was developed over a flat plate model. An adjustable NACA 0012 airfoil was placed above the flat plate to produce adverse and favorable pressure gradients (APG and FPG) at the measurement position. With a free-stream flow velocity between 15 and 60 m/s, the range of Reynolds numbers, $1500 < Re_\theta < 11400$, was covered in the measurement.

The wall pressure spectra were measured using sensors of different sizes, types, and mounting configurations, that is, flush- and pinhole-mountings. Based on the reference spectra measured with a pinhole-mounted sensor, the attenuation spectra for different sensors were calculated, and the results show that the attenuation is larger for sensors with a larger sensing area and for a flow with a lower free-stream velocity. Furthermore, it was demonstrated that an APG increases the attenuation significantly, whereas a FPG has no noticeable effect on the attenuation.
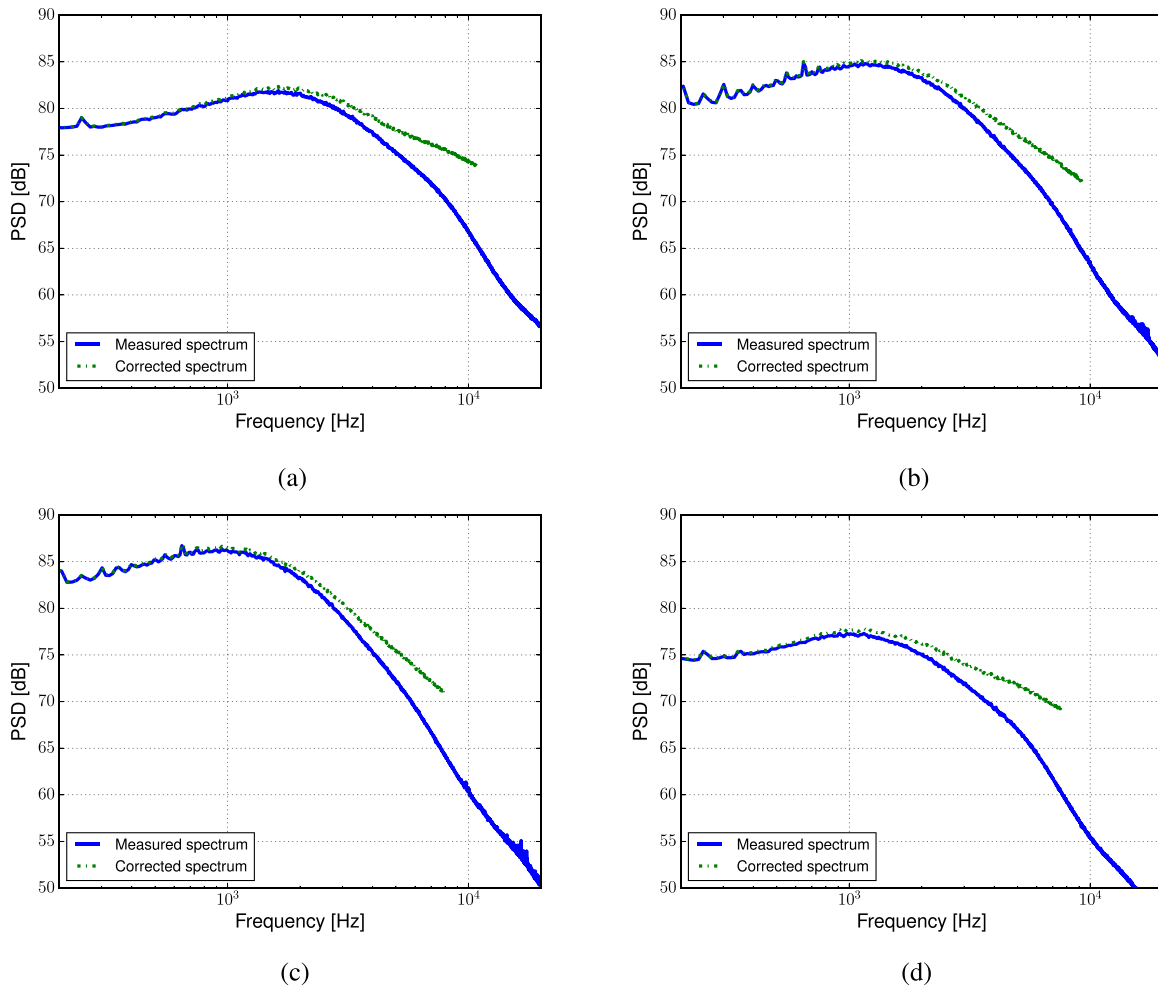
**FIG. 17.** Measured and corrected wall pressure spectra for the NACA test cases[42] listed in Table II, (a) AOA = 0° with $U_e$ = 52.3 m/s; (b) AOA = 4° with $U_e$ = 51.6 m/s; (c) AOA = 6° with $U_e$ = 50.1 m/s; and (d) AOA = 0° with $U_e$ = 35.4 m/s.

According to Corcos,[1] the sensor radius $r$ and the convection velocity $U_c$ are the key parameters for calculating the attenuation. In practice, non-uniform sensitivity over the sensor surface which was not considered by Corcos can significantly reduce the effective sensing area. This issue was discussed from the theoretical point of view, and the effective radius of sensors was suggested.

Furthermore, the fact that $U_c$ depends on the flow condition and convection distance[7,8] is of great importance for determining the attenuation. A convection velocity model was proposed, including the Reynolds number and pressure gradient effects. A scaling factor for the distance dependence was suggested to determine $U_c$ applied to different sensor sizes.

Finally, a correction model as a function of TBL-dependent parameters was proposed, which can be applied to a wide range of flow conditions and commonly used sensor types. To assess the present correction model, four test cases were selected which were measured at different facilities with different sensor types, covering a wide range of Reynolds numbers ($1.6 \times 10^3 < Re_\theta < 1.19 \times 10^5$).
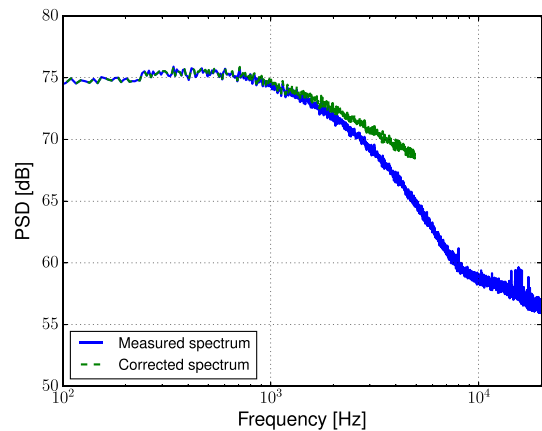


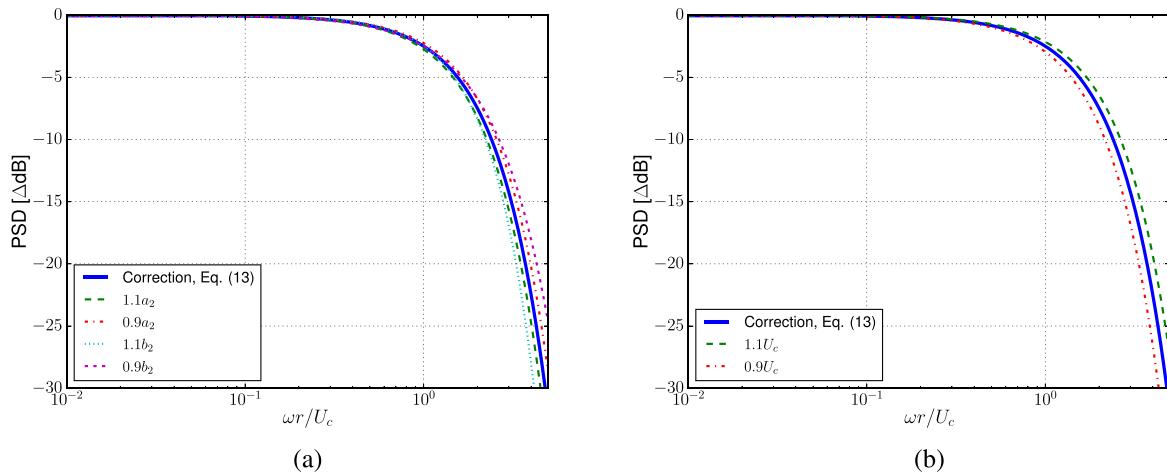**FIG. 18.** Measured and corrected wall pressure spectra for the car test case[43] listed in Table II.

FIG. 19. Uncertainty estimation of the correction based on, (a) uncertainty in the variables of Eq. (13); and (b) uncertainty in $U_c$.

The results show that spectral attenuation can be corrected with the model by more than 20 dB with high accuracy.

## AUTHOR DECLARATIONS

### Conflict of Interest

The authors have no conflicts to disclose.

### Author Contributions

**Nan Hu:** Data curation (lead); Investigation (lead); Validation (lead); Writing – original draft (lead).

## DATA AVAILABILITY

The data that support the findings of this study are available from the corresponding author upon reasonable request.

## APPENDIX A: HELMHOLTZ RESONANCE OF THE MOUNTED SENSORS

To measure the Helmholtz resonance and the transfer function of the applied sensors, a laser sound source was used. The source was generated by the expansion of a plasma, which was produced by focusing the high energy laser beam on a small spot.[47,48] Based on the monopole-like directivity of the source, the sound pressure measured at different positions is of the same magnitude when the distance correction is taken into account.[48] Thus, the source can also be used for the sensor calibration after mounting, correcting the small uncertainty of the calibration beforehand and the possible effect due to the individual mounting configuration.

Figure 20(a) shows the sound pressure spectra measured with the sensors located at $x = 1170$ mm, which are averaged spectra based on more than a hundred laser pulses. Taking the 1/8-in. microphone as reference, the spectral magnitude is adjusted within a range of $\pm 0.3$ dB to achieve the best fit below 6 kHz where no effect of the resonance or the attenuation is expected. These obtained adjustment values are also applied to the measured wall pressure spectra in the present work for the analysis of the attenuation spectra.

The result shows that the resonance of the pinhole-mounted sensors, and also, the Kulite sensors with B-screen can be accurately determined. To calculate the corresponding transfer function, the spectrum measured with the Kulite sensor without screen is taken as a reference assumed to have no attenuation due to its small size. This assumption is expected to be true at least below 50 kHz because the sensing area (chip size of 1 mm$^2$) of the Kulite sensor is much smaller than the 1/8-in. microphone and the attenuation measured by the 1/8-in. microphone is only observable at frequencies larger than 35 kHz.

The obtained transfer functions are plotted in Fig. 20(b), along with fitting curves determined with the following expression:[49]

$$H(f) = \frac{1}{1 + \frac{i}{q}(f/f_r) - (f/f_r)^2}, \quad (A1)$$

where $q$ is the quality factor and $f_r$ is the resonance frequency. The fitting curves are in good agreement with the measurement results. The obtained curves are used in the present work to correct the measured wall pressure spectra.

## APPENDIX B: DISTANCE DEPENDENCE OF THE CONVECTION VELOCITIES

Figure 21(a) shows the convection velocities for different sensor separations, measured with $U_\infty = 30$ m/s in ZPG. The velocity is calculated with $U_c(\omega, \Delta x) = \Delta x \, \omega / \theta(\omega, \Delta x)$, where $\theta(\omega, \Delta x)$ is the phase difference with a streamwise separation of $\Delta x$. The result shows that the magnitude of the velocity spectra increases with a
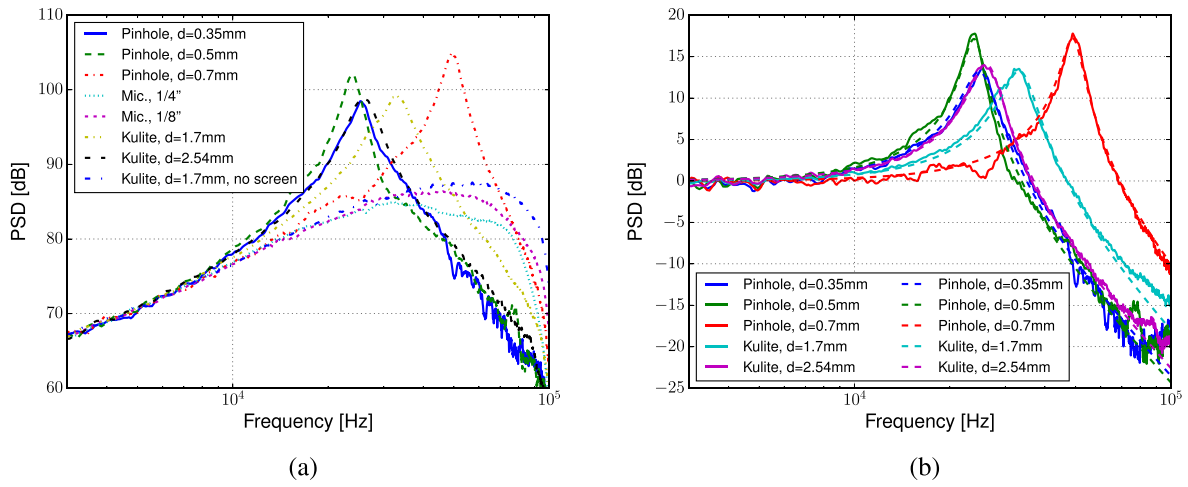
**FIG. 20.** (a) Sound pressure spectra measured at $x = 1170$ mm; and (b) transfer functions, (dashed line) measured spectra, and (dotted line) fitting curves.



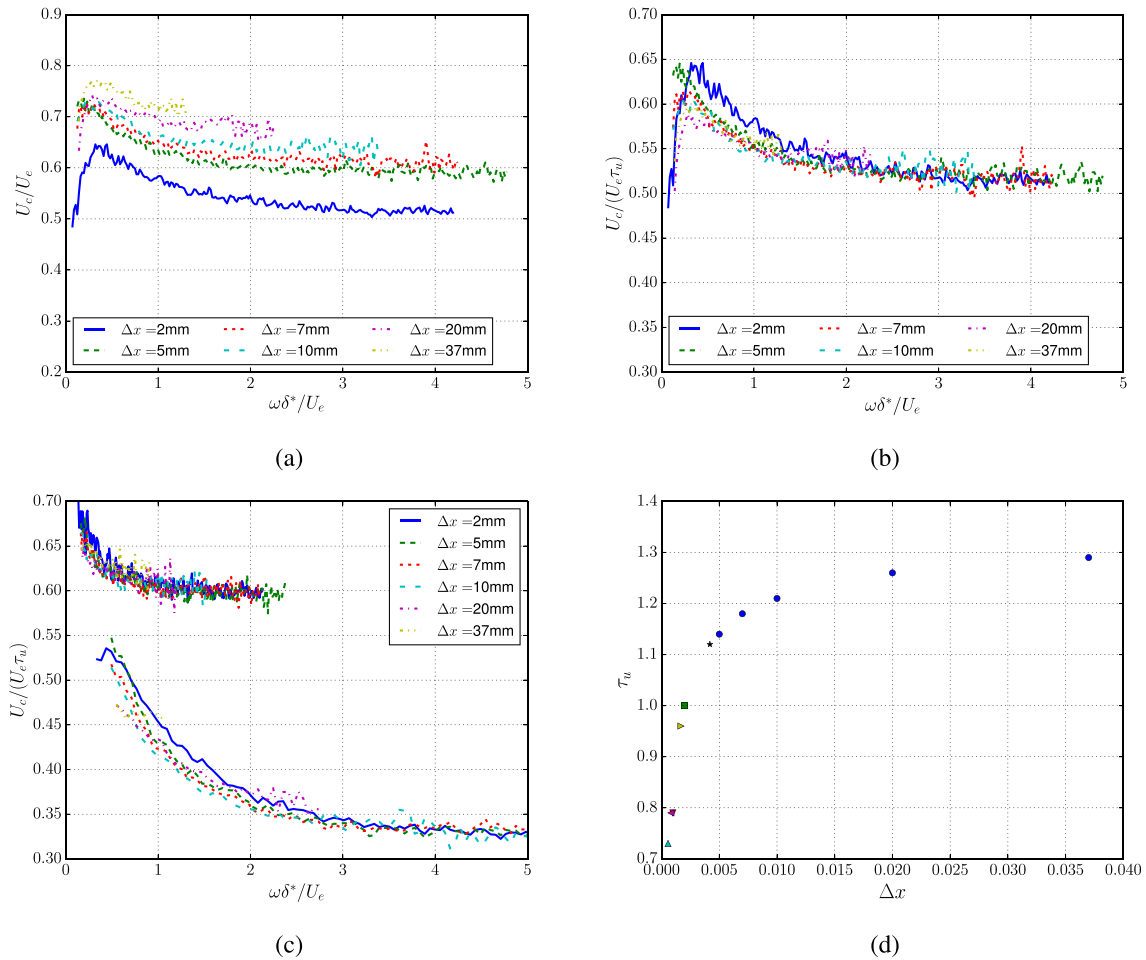**FIG. 21.** (a) Convection velocities with $U_\infty = 30$ m/s in ZPG; (b) scaling of the convection velocities with $U_\infty = 30$ m/s in ZPG; (c) scaling of the convection velocities with $U_\infty = 30$ m/s in APG 12° (smaller values) and FPG −12° (larger values); (d) scaling factors; ■, 1/4″ microphone; ▼, 1/8″ microphone; ▲, Kulite with $d = 1.7$ mm; ◄, Kulite with $d = 2.54$ mm; ►, GRAS 48LA; ★, B&K 4948.

larger $\Delta x$. This is because the smaller eddies moving with a lower velocity die out over a shorter distance. Consequently, at the larger distance, the obtained velocity is rather attributed to the larger eddies moving with a higher velocity.

Interestingly, the velocity spectra shape with different separations seems to be comparable. Figure 21(b) shows that, with a scaling factor $\tau_u$, the velocity spectra collapse to $U_c(\omega, \Delta x = 2$ mm) with only a small discrepancy at lower frequencies. This feature also holds for flows with pressure gradients. Figure 21(c) shows the collapse of the velocity spectra for an APG and a FPG cases scaled with the same values of $\tau_u$ used for the ZPG case, which are plotted in Fig. 21(d). Furthermore, Fig. 21(d) shows the estimated values for the different sensors used in the present test, which are obtained through scaling the measured attenuation spectra. The values for two other microphones used for the application cases, that is, GRAS 48LA and B&K 4948, are estimated based on the development trend of $\tau_u$. For convenience, $\tau_u = 1$ (for $U_c$ with $\Delta x = 2$ mm) is used for the 1/4-in. microphone with the active membrane radius of $r = 2.15$ mm. This introduces a scaling factor of 0.93, that is, $\Delta x = 0.93\, r$, which is applied to all the sensors shown in Fig. 21(d) because the sensors are referenced to the 1/4-in. microphone.

# REFERENCES

[1]G. M. Corcos, "Resolution of pressure in turbulence," J. Acoust. Soc. Am. **35**(2), 192–199 (1963).

[2]M. K. Bull and A. S. W. Thomas, "High frequency wall-pressure fluctuations in turbulent boundary layers," Phys. Fluids **19**, 597–599 (1976).

[3]G. Schewe, "On the structure and resolution of wall-pressure fluctuations associated with turbulent boundary-layer flow," J. Fluid Mech. **134**, 311–328 (1983).

[4]W. L. Keith, D. A. Hurdis, and B. M. Abraham, "A comparison of turbulent boundary layer wall-pressure spectra," J. Fluids Eng. **114**, 338–347 (1992).

[5]R. M. Lueptow, "Transducer resolution and the turbulent wall pressure spectrum," J. Sound Vib. **97**, 370–378 (1995).

[6]S. P. Gravante, A. M. Naguib, C. E. Wark, and H. M. Nagib, "Characterization of the pressure fluctuations under a fully developed turbulent boundary layer," AIAA J. **36**(10), 1808–1816 (1998).

[7]T. M. Farabee and M. J. Casarella, "Spectral features of wall pressure fluctuations beneath turbulent boundary layers," Phys. Fluids **3**(10), 2410–2420 (1991).

[8]N. Hu and M. Herr, "Characteristics of wall pressure fluctuations for a flat plate turbulent boundary layer with pressure gradients," AIAA Paper No. 2016-2749, 2016.

[9]J. V. Blitterswyk and J. Rocha, "An experimental study of the wall-pressure fluctuations beneath low Reynolds number turbulent boundary layers," J. Acoust. Soc. Am. **141**(2), 1257–1268 (2017).

[10]P. Jaiswal, S. Moreau, F. Avallone, D. Ragni, and S. Pröbsting, "On the use of two-point velocity correlation in wall-pressure models for turbulent flow past a trailing edge under adverse pressure gradient," Phys. Fluids **32**, 1–27 (2020).

[11]M. Szőke, D. Fiscaletti, and M. Azarpeyvand, "Uniform flow injection into a turbulent boundary layer for trailing edge noise reduction," Phys. Fluids **32**, 1–14 (2020).

[12]R. B. Gilchrist and W. A. Strawderman, "Experimental hydrophone-size correction factor for boundary layer pressure fluctuations," J. Acoust. Soc. Am. **38**, 298–302 (1965).

[13]P. H. White, "Effect of transducer size, shape, and surface sensitivity on the measurement of boundary layer pressure," J. Acoust. Soc. Am. **41**, 1358–1363 (1967).

[14]F. E. Geib, "Measurements on the effect of transducer size on the resolution of boundary-layer pressure fluctuations," J. Acoust. Soc. Am. **46**, 253–261 (1969).

[15]P. V. Bruel and G. Rasmussen, "Free-field response of condenser microphones," Technical Report No. TR 1-1959 (Bruel Kjaer, 1959).

[16]H. H. Schloemer, "Effects of pressure gradients on turbulent-boundary-layer wall-pressure fluctuations," J. Acoust. Soc. Am. **42**(1), 93–113 (1967).

[17]M. R. Catlett, J. M. Anderson, J. B. Forest, and D. O. Stewart, "Empirical modeling of pressure spectra in adverse pressure gradient turbulent boundary layers," AIAA J. **54**(2), 569–587 (2016).

[18]N. Hu and L. Erbig, "Effect of sensor mounting and flow history on measured wall pressure spectra," AIAA J. **58**(7), 2964–2974 (2020).

[19]P. Zhou, Q. Liu, S. Zhong, Y. Fang, and X. Zhang, "A study of the effect of serration shape and flexibility on trailing edge noise," Phys. Fluids **32**, 1–15 (2020).

[20]M. Herr, "Design criteria for low-noise trailing-edges," AIAA Paper No. 2007-3470 (2007).

[21]H. M. Nagib, K. A. Chauhan, and P. A. Monkewitz, "Approach to an asymptotic state for zero pressure gradient turbulent boundary layers," Philos. Trans. R. Soc., A **365**, 755–770 (2007).

[22]N. Hu, "Assessment of miniature Knowles sensor for the measurement of wall pressure fluctuations," in DAGA, 2020.

[23]D. B. Spalding, "A single formula for the law of the wall," J. Appl. Mech. **28**, 455–457 (1961).

[24]M. Ji and M. Wang, "Surface pressure fluctuations on steps immersed in turbulent boundary layers," J. Fuild Mech. **712**, 471–504 (2012).

[25]M. Esteve, P. Reulet, and P. Millan, "Flow field characterisation within a rectangular cavity," in *10th International Symposium on Applications of Laser Techniques to Fluid Mechanics, Portugal* (2000).

[26]A. Golubev and S. Kuznetsov, "Wall pressure fluctuations on the surface of sloped forward-facing steps," AIAA J. **58**(10), 4595–4599 (2020).

[27]M. Roger, "Microphone measurements in aeroacoustic installations," in *Design and Operation of Aeroacoustic Wind Tunnel Tests for Ground and Air Transport STO-AVT-287* (Von Karman Institute for Fluid Dynamics, 2017).

[28]N. A. Balantrapu, R. J. Repasky, L. A. Joseph, and W. J. Devenport, "The dynamic response of a pinhole microphone under flows of varying shear stress," AIAA Paper No. 2018-3933, 2018.

[29]D. Fritsch, V. Vishwanathan, K. T. Lowe, and W. J. Devenport, "The effect of grazing flow on pinhole condenser microphones," AIAA Paper No. 2021-0130, 2021.

[30]M. C. Goody, "Empirical spectral model of surface pressure fluctuations," AIAA J. **42**(9), 1788–1794 (2004).

[31]W. W. Willmarth and C. E. Wooldridge, "Measurements of the fluctuating pressure at the wall beneath a thick turbulent boundary layer," J. Fluid Mech. **14**, 187–210 (1962).

[32]G. M. Corcos, "The structure of the turbulent pressure field in boundary layer flows," J. Fluid Mech. **18**, 353–378 (1964).

[33]A. Smol'yakov and V. Tkachenko, "Model of a field of pseudosonic turbulent wall pressures and experimental data," Akust. Zh. **37**, 1199–1207 (1991).

[34]D. J. J. Leclercq and X. Bohineust, "Investigation and modelling of the wall pressure field beneath a turbulent boundary layer at low and medium frequencies," J. Acoust. Soc. Am. **257**(3), 477–501 (2002).

[35]N. Hu, "Coherence of wall pressure fluctuations in zero and adverse pressure gradients," J. Sound Vib. **511**, 1–27 (2021).

[36]W. K. Blake, *Mechanics of Flow-Induced Sound and Vibration*, 1st ed. (Academic Press, Inc., 1986).

[37]A. Smol'yakov, "A new model for the cross spectrum and wavenumber-frequency spectrum of turbulent pressure fluctuations in a boundary layer," Acoust. Phys. **52**(3), 331–337 (2006).

[38]Y. Rozenberg, G. Robert, and S. Moreau, "Wall-pressure spectral model including the adverse pressure gradient effects," AIAA J. **50**(10), 2168–2179 (2012).

[39]N. Hu, "Empirical model of wall pressure spectral in adverse pressure gradients," AIAA J. **56**(9), 3491–3506 (2018).

[40]W. J. Devenport and K. T. Lowe, "Equilibrium and non-equilibrium turbulent boundary layers," Prog. Aerosp. Sci. **131**, 1–50 (2022).

[41]A. Klabes, C. Appel, M. Herr, and M. Bouhaj, "Fuselage excitation during cruise flight conditions: Measurement and prediction of pressure point spectra," AIAA Paper No. 2015-3115, 2015.

[42]A. Herrig, "Validation and application of a hot-wire based method for trailing edge noise measurements on airfoils," Ph.D. thesis (University of Stuttgart, 2012).

[43]L. Erbig and M. Maihöfer, "A hybrid RANS/LES for automotive gap noise simulations," AIAA Paper No. 2019-2445, 2019.

[44]N. Hu, C. Appel, S. Haxter, S. Callsen, and A. Klabes, "Simulation of surface pressure fluctuations on an Airbus-A320 fuselage at cruise conditions," AIAA J. **59**(5), 1585–1597 (2021).

[45]M. Herr, R. Ewert, C. Rautmann, M. Kamruzzaman, D. Bekiropoulos, A. Iob, R. Arina, P. Batten, S. Chakravarthy, and F. Bertagnolio, "Broadband trailing-edge noise predictions—Overview of BANC-III results," AIAA Paper No. 2015-2847, 2015.

[46]A. Herrig, M. Kamruzzaman, W. Würz, and S. Wagner, "Broadband airfoil trailing-edge noise prediction from measured surface pressures and spanwise length scales," Int. J. Aeroacoust. **12**, 53–82 (2013).

[47]K. S. Rossignol, J. Delfs, and F. Boden, "On the relevance of convection effects for a laser-generated sound source," AIAA Paper No. 2015-3146, 2015.

[48]K. S. Rossignol and J. Delfs, "Analysis of the noise shielding characteristics of a NACA0012 2D wing," AIAA Paper No. 2016-2795, 2016.

[49]E. Salze, C. Bailly, O. Marsden, E. Jondeau, and D. Juvé, "An experimental characterisation of wall pressure wavevector-frequency spectra in the presence of pressure gradients," AIAA Paper No.2014-2909, 2014.